Preparation of Materials for Deep Tissue Imaging with Slow Light

Master Thesis

Mengqiao Di

Supervisor: Prof. Stefan Kröll

Division of Atomic Physics
Department of Physics
Lund University

Lund 2018 Spring
Lund Reports on Atomic Physics, LRAP-545

LUND
UNIVERSITY

Abstract

Ultrasound Optical Tomography (UOT) is a proposed technique, which combines ultrasound imaging and optical imaging in a new way to detect, e.g., blood oxygenation and tumors deep inside biological tissue, where the ultrasound provides an excellent spatial resolution, and the optical imaging gives a high contrast of different tissues according to optical properties. However, the challenges of this technique are it is hard to subtract the UOT signal from the background (diffracted light) since the UOT signal is much weaker than the background light and they are quite close in the frequency domain. Thus, a narrow band filter with a high suppression ratio is needed. Moreover, it is crucial for developing and evaluating UOT to make phantoms to mimic the properties of human tissues, and also to be able to measure the exact optical properties of the phantoms. Testing that the light propagation inside the phantoms matches Monte Carlo (MC) simulation is also necessary since Monte Carlo simulation can be used to simulate the realistic conditions of the UOT experiments in the future.

In this thesis, the phantoms with a specific scattering coefficient and absorption coefficient were made by using diluted Indian ink, Intralipid 20%, and distilled water. Two spectroscopic absorption methods were used including direct absorption spectroscopy and photon time-of-flight spectroscopy. The direct absorption spectroscopy with 11% variation was used to validate the photon time-of-flight spectroscopy which can provide the scattering coefficient of the phantoms as well. With the help of the full control of the absorption coefficient and scattering coefficient, the measurement result of the light intensity transmitted through the phantoms as a function of scattering and absorption coefficient matched Monte Carlo simulations. Furthermore, a rare-earth doped crystal can be used as a spectral filter to improve the signal to background ratio (SNB). The spectral filter was burned and probed using a strongly absorbing polarization direction in the crystal. The burning procedure was decided based on simulations to give sharp edges and a good suppression between the transmission inside the center of the spectral hole and outside the spectral hole 1.5 MHz away. A 50.4 dB suppression for a 1 MHz spectral hole was achieved by optimizing the pulse parameters. The slow light effect generated inside the spectral filter can delay the UOT signal 2 μs from the background in the time domain. The lifetime of the spectral hole can be extended to more than half a minute by adding a small magnetic field of 10 mT.

For the future, it is proposed that a better spectral hole with a higher suppression and shaper edges can be obtained by improving the hole burning technique. In addition, other absorbers and scatterers can also be investigated to make long-lived phantoms in the future.

Popular Science

Are you curious about why you feel hot after lying outside for a while under the sunshine? When you work at night with the light on, do you wonder how the light bulb emits light? What's more, have you seen the beautiful aurora in the north of Sweden? All of these happen due to the light-matter interaction!

People are familiar with light, no matter whether it is natural light, e.g., the aurora or artificial light, e.g., LED light. When light meets different matters, different romantic stories (interaction) happen. This project tells a story between light and a crystal doped by rare-earth ions. However, the story only happens when light meets the matter under the right condition in a similar way as you cannot see aurora frequently.

When light with a frequency close to the transition of rare-earth ions goes through the crystal, it will be absorbed. Then the rare-earth doped crystal acts as a band-pass filter which can have a variable narrow passband for the incident light. But how does it work? It will absorb the incident light but let the light with the same frequency as the passband go through. Hence, the crystals select the same frequency as its passband. How is this passband created? In brief, a passband is created inside a praseodymium (Pr) doped Y_2SiO_5 crystal with light which has the same frequency as the passband we want to create. The light is used to burn away the ions in the passband. Thus, when it is irradiated by the light at the same frequency, there are no longer any ions absorbing it (no story will happen). Moreover, this type of special filter will create another story, which is called "slow light effect". To make the story short, it is a time delay of the light like the way electrical pulses delayed in a band-pass filter in electrical circuits.

Why do we need such filters? Well, our filter can slow down the light by 4 to 5 orders of magnitude! The slowed down light can be widely used in quantum memories, laser stabilization, and deep tissue imaging, etc.

Acknowledgements

First of all, I would like to express my sincere appreciation to my supervisor Professor Stefan Kröll for giving me a learning opportunity to work in this group and always being patient to my stupid questions and giving a lot of constructive advice. Thank you for all the discussions which make me learn how to solve problems. Thank you for the time and the effort you put, which have greatly enhanced my understanding of physics.

Special thanks to my partner Meng Li for all the help in two years. You helped me a lot for all the courses, reports even troubles in daily life especially when I just came to Sweden. Thanks for your support all the time and I have learned a lot from you.

I would like to thank all the people in the group: Chunyan Shi, Alexander Bengtsson, Sebastian Horvath, Qian Li and Adam Kinos for all the discussions and help during the thesis time. Thank them for helping me with the control of the equipment in the lab and the experimental setup. Also, all the wonderful ideas came up for a better setup.

It is a great honor to do my thesis in Atomic Physics especially in this group. Special thanks to Nina Reistad for teaching me how to make phantoms and the direct absorption spectroscopy setup. Thank you so much for giving me a chance to see the clinical surgeries, and it is a great honor and pleasure for me to feel how the photoacoustic tomography work as a patient.

I would also like to thank my friends Yuhe Zhang, Wensi Zhu and Chunyan Shi, for the relaxing time during the lunch, and always be with me and support me in daily life.

Last but not the least, I wish to thank my mama, Xiuhong Zhao, for the endless love and guidance, who always tell me the most important thing is to live a happy life.

Abbreviations

AOTF	**A**cousto-**O**ptical **T**unable **F**ilter
AOM	**A**cousto-**O**ptic **M**odulator
AWG	**A**rbitrary **W**avefront **G**enerator
CFD	**C**onstant **F**raction **D**iscriminator
DE	**D**iffusion **E**quations
ESR	**E**nhanced **S**pecular **R**eflector
IRF	**I**nstrumental **R**esponse **F**unction
MC	**M**onte **C**arlo
MCA	**M**ulti-**C**hannel **A**nalyzer
MCML	**M**onte **C**arlo **M**ulti-**L**ayered
MFP	**M**ean **F**ree **P**ath
MRI	**M**agnetic **R**esonance **I**maging
PEEK	**P**olyether **E**ther **K**etone
PTOF	**P**hoton **T**ime-**O**f-**F**light
REE	**R**are-**E**arth **E**lements
RRT	**R**adiative **T**ransport **T**heory
SCLFC	**S**uper **C**ontinuum **L**aser **F**iber **S**ource
TAC	**T**ime to **A**mplitude **C**onverter
TCSPC	**T**ime-**C**orrelated **S**ingle **P**hoton **C**ounting
UOT	**U**ltrasound **O**ptical **T**omography
WMC	**W**hite **M**onte **C**arlo

Contents

Chapter 1

Introduction

Recently rare-earth spectral filters using the hole burning technique have shown attractive applications in different areas, such as quantum memories [1], laser stabilization [2], and optical detection of the blood oxygenation in the heart and brain [3]. Usually, these spectral filters are made from inorganic crystals doped by rare-earth ions. These ions can be transferred by laser light to the states where they do not absorb light anymore, which are called auxiliary states. When light propagates through this narrow spectral transmission window within a highly absorbing frequency region, it will experience a time delay due to the strong dispersion [4] in a similar manner to that when the electrical pulses go through a band-pass filter in electrical circuits. The strong dispersion phenomenon occurs since the refractive index changes dramatically with the frequency in the transparent window. Then it causes the group velocity to be slower than the light phase velocity. This phenomenon is called the slow light effect. The slow light effect can be enhanced when there is a significant decrease in the group velocity, as is the case for a narrow transmission window. In our cases, a spectral filter made by doping 0.05% praseodymium into a Y_2SiO_5 crystal based on an optical hole burning technique creates a passband of 1-2 MHz, and the speed of light is slowed down by a factor of 10^4-10^5 compared to in vacuum [5].

The work in this thesis is motivated by developing the Ultrasound Optical Tomography (UOT) technique, which is a medical imaging technique developed for being used inside the human body assessing the blood oxygenation, e.g., at heart and brain with high resolution and high contrast. Optical imaging can provide different optical properties of different tissue with the potential of remote detection and non-invasive imaging. The ultrasound provides spatial resolution, and when light penetrates through the ultrasound focus, the light frequency can be shifted from the original light frequency because of the acousto-optical effect caused by the laser and the ultrasound passing through the tissue at the same time. Thus two side-bands with ultrasound tagged frequencies (f_l-f_{us} and f_l+f_{us}) are generated as shown in Figure 1.1. When the tumor is located at the focus of the ultrasound, the generated sidebands will be absorbed compared to what it would be like without a tumor. Thus the images of deep tissue such as the heart and the brain can be obtained by monitoring the intensity of the sidebands which are also called the UOT signal. However, the difficulties are that the UOT signal is quite weak since only a small amount of light penetrates through the ultrasound focus, and then only a fraction of this becomes UOT signal. The UOT signal is much weaker than the non-frequency-shifted light, and they are quite close to each other in the frequency domain. The closeness is due to the ultrasound having to operate around 1.5 MHz. So a spectral filter was made to extract the weak UOT signal from a much stronger background. It will let one of the side-bands pass through, and absorb the non-frequency-shifted light. The generated slow light effect inside the spectral filter can delay the UOT signal from the background in the time domain. This is how the spectral filters are used to improve the signal-to-background ratio.

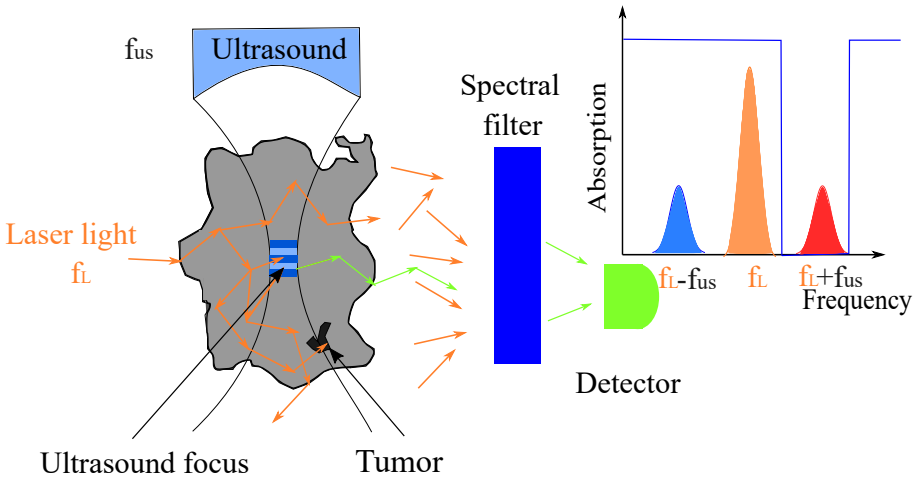

Figure 1.1: The scheme of Ultrasound Optical Tomography.

This thesis mainly includes three parts of work: the first part intended to make phantoms with specific absorption coefficient and scattering coefficient to mimic the human tissue. The second part is to investigate whether the measurement results of the light intensity and the distribution inside the tissue match Monte Carlo simulations. The third part is the generation of a spectral filter, with the slow light effect using the spectral hole burning technique, has been implemented theoretically and experimentally. The third part is one of the most crucial parts of the UOT scheme since it improves the signal to background ratio.

Chapter 2 outlines the relevant optical properties of the phantoms, for example, the interaction between light and turbid media can be described by radiative transport theory, which models the condition of multiple scattering. Subsequently, the diffusion theory and Monte Carlo method, the solutions to the radiative transport theory, are also presented in this chapter. Furthermore, the spectroscopic properties of rare-earth-ion-doped crystals are depicted, and the Maxwell-Bloch equations and the Bloch sphere are used as explanations for the coherent interaction between light and atoms which are approximated by a two-level system. At last, the results of the Monte Carlo simulation and the Spectral hole burning simulation are shown for the preparation of the experiments.

Chapter 3 describes different spectroscopic approaches for determining the optical properties of phantoms, testing how the propagation of light in phantoms matches the Monte Carlo simulation and burning a spectral hole. Moreover, the equipment used in the experiments are discussed here. It is of importance to illustrate how the technical issues are solved.

Chapter 4 discusses the comparable results obtained from direct absorption spectroscopy and photon time-of-flight spectroscopy, and the identical ones from transmitted light in phantoms and Monte Carlo simulations. How good the spectral hole is and how the magnetic field effects it are also investigated. Meanwhile, the qualitative analysis of the results is shown in this chapter.

Finally, the conclusions and the improvements that can be done in the future are carried out in Chapter 5.

Chapter 2

Theory

2.1 Scattering and absorption of materials

2.1.1 Scattering

Scattering occurs when light propagates through an inhomogeneous medium, which can be described by the interaction between electromagnetic radiation and scatters. In this thesis, only elastic scattering is concerned since inelastic scattering is quite weak, i.e. Raman scattering, as compared to elastic scattering. In the elastic scattering process, the energy conservation is fulfilled, which implies the wavelength doesn't change. Considering the density of the scatters, there are two types of scattering. One is single scattering, which means the light is diffused by a few scatterers and the backscattering is negligible. A coarse assumption is made for single scattering that the scattered light is imperceptible as compared to the transmitted light as shown in Figure 2.1 (left), and single scattering can be used to simplify complicated problems. An intuitive example for single scattering is the blue sky. The reason for the blue sky was provided by Rayleigh, when the particles are much smaller than the wavelength of the light and the scattering cross section is wavelength-dependent with a relation: $\sigma_{\text{sca}} \propto \lambda^{-4}$ [6]. Thus the blue light with a shorter wavelength is scattered more than the red light with a longer wavelength. Single scattering generally exists when the light propagates through the earth atmosphere as well as the interstellar atmosphere [7]. Figure 2.1 (right) shows multiple scattering, which indicates that the light is scattered multiple times by dense scatters in the sample. All the transmitted light comes from the scattered light. There are a lot of multiple scattering examples existing in our daily life such as white clouds, milk, and snow.

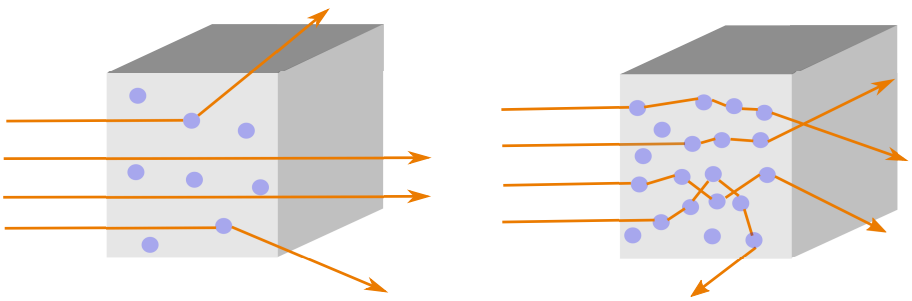

Figure 2.1: The left one shows the light is only scattered once by each particle while the right one illustrates the light is deflected by scatters multiple times. The difference between two media is the density of the scatters.

The scattering of biological tissue is quite complicated since different molecules have different

properties. However, multiple scattering theory works for biological tissue from the point of view of light-matter interaction [8]. A few optical parameters are used to depict the properties of tissue. The interaction strength between light and scatters can be described by scattering cross section σ_{sca}, which is related to the refractive index difference between the scattering medium and the surrounding. The refractive index of tissue normally is 1.4 for light with the wavelength of 600 nm-1000 nm [9]. One of the most common parameters for describing the average property of tissue is the scattering coefficient, μ_s (cm^{-1}), which gives the interaction probability of the scatters per unit length. The scattering coefficient of tissue can be estimated by using Mie theory as below when the shape of scatters is spherical [9].

$$\mu_s = a\lambda^{-b}, \tag{2.1}$$

where the coefficients a and b are different due to the different particle size distribution and the density of the scatters [9]. For the Intralipid 20% used in this thesis to make phantoms, the coefficients a and b can be found in [10]. The angular distribution of scattered light inside tissue is given by scattering phase function $p(\hat{s}', \hat{s})$, which depicts the probability from initial propagation direction $\hat{s}'$ to a new direction $\hat{s}$. Figure 2.2 gives an intuitive picture of scattering phase function, and the scattering probability only depends on deflection angle, θ assuming that it is symmetric for the azimuthal angle, ψ. That is, $p(\hat{s}', \hat{s}) = p(\cos(\theta))$. The anisotropic factor g, g=$\langle \cos\theta \rangle$, is introduced to describe the probability of scattered light in the forward direction. So a scattering phase function related to g factor is created by Henyey and Greenstein [11], which approximates multiple scattering of spherical scatters (Mie scatters), and the dominant process is forward scattering.

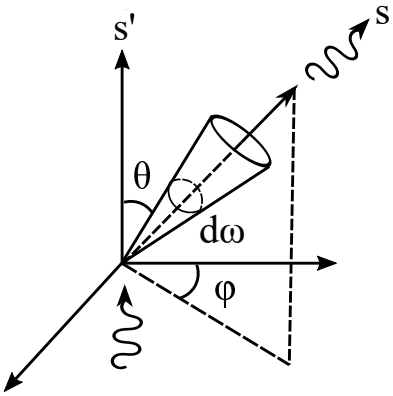

Figure 2.2: The geometry of the scattering phase function, which gives the probability of the propagation along s' direction deflecting into s direction.

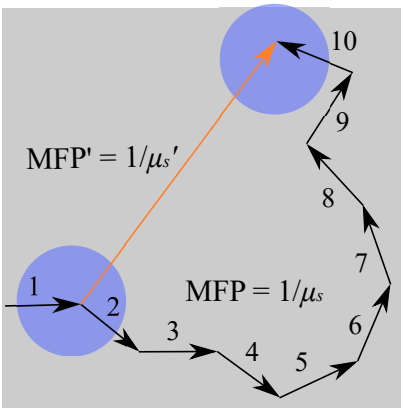

Figure 2.3: Ten mean free path (MFP) $1/\mu_s$ with different scattering angles is identical to to one reduced mean free path (MFP$'$) which is the reciprocal of μ_s'.

$$p(\theta) = \frac{1}{4\pi} \frac{1 - g^2}{(1 + g^2 - 2g\cos(\theta))^{3/2}}. \tag{2.2}$$

Combining the g-factor and scattering coefficient, the reduced scattering coefficient is introduced:

$$\mu_s' = (1 - g)\mu_s, \tag{2.3}$$

where the μ_s' tells how much light is totally deflected to a new direction. The inversion of it is the reduced mean free path (MFP) which indicates the distance of light traveling until a new scatter as shown in Figure 2.3. The reduced scattering coefficient of Intralipid 20% is subjected to

$$\mu_s'(\lambda) = y_0 + a \cdot \lambda + b \cdot \lambda^2, \tag{2.4}$$

where y_0, a and b are known and given in [10].

2.1.2 Absorption

Another critical process, when the light transmits through the medium, is absorption. Since only elastic scattering is concerned in this thesis, the fluorescence process is not considered. The description of the absorption process is the absorption coefficient, μ_a (cm^{-1}), which is also a wavelength dependent parameter and can be expressed as:

$$\mu_a(\lambda) = \sigma_{\mathrm{abs}}(\lambda)\rho_{\mathrm{abs}} \tag{2.5}$$

where σ_{abs} is the absorption cross section at wavelength λ, and ρ_{abs} is the density of absorbers. Similar to the scattering coefficient, the absorption coefficient gives the strength of absorption per unit length. Moreover, the intensity of the transmitted light is given by the Beer-Lambert law:

$$I = I_0 \exp(-\mu_a L) \tag{2.6}$$

where I_0 is the intensity of the incident light and L is the distance light traveled.

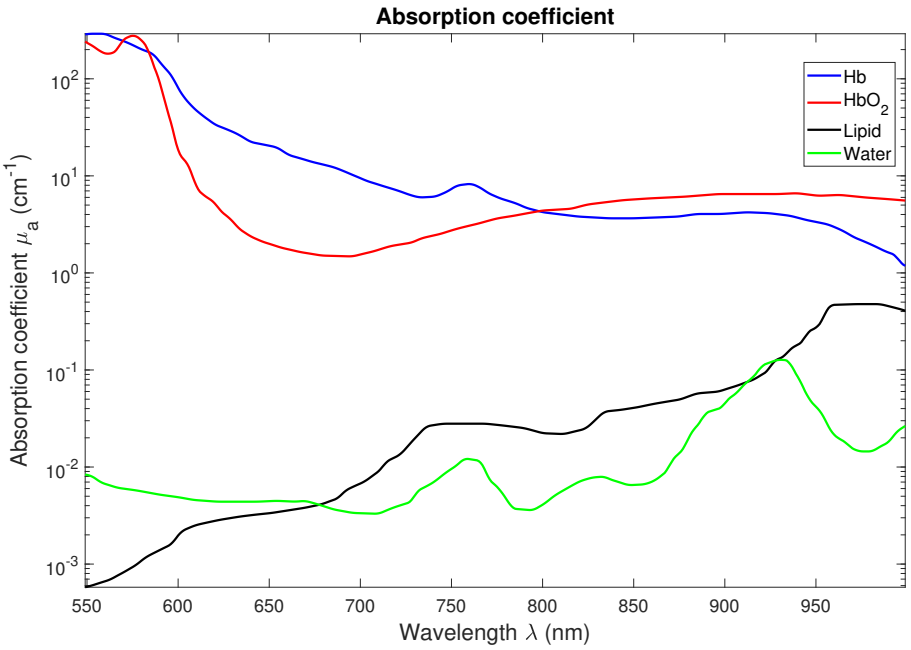

Figure 2.4: The tissue optical window and the absorption coefficient of the oxygenated hemoglobin [12], deoxygenated hemoglobin [12], lipids [13] and water [14] at different wavelength

The high absorption inside tissue limits the penetration depth of the light in the ultraviolet spectrum. Nonetheless, in part of the visible and infrared spectral range, a relatively low absorption can be obtained inside the tissue, which is called the tissue optical window [15] as shown in Figure 4.4. For the visible part (λ< 600 nm), the hemoglobin in the blood absorbs light strongly while for the infrared part (λ> 1000 nm), the light is mainly absorbed by water. Some of the main chromophores such as oxyhemoglobin, de-oxyhemoglobin, water, and lipid which are used as scatters to make phantoms, are shown in this figure. The prominent absorption in this optical window comes from: water [14], hemoglobin [12], myoglobin[16], lipids [13], cytochromes [17], melanin [18], and collagen [19]. However, none of them absorb strongly, and there are plenty of therapeutic applications in the optical tissue window due to comparably low absorption.

2.1.3 Solutions to the radiative transport equation

2.1.3.1 Diffusion theory

One of the approximate solutions of the radiative transport equation (RTE) is the diffusion equation (DE), which a good model for the light propagation inside the medium. The RTE is explained in Appendix A. Diffusion theory is a simplified approach to give a not time-consuming numerical or even analytical solution. More simplifications and assumptions are provided in [7].

However, the validity of the diffusion theory is limited. When the medium has a strong absorption or weak scattering, diffusion theory breaks down. Only the scattering prominent medium ($\mu_s' \gg \mu_a$) works for diffusion theory, and the solutions are plausible only far away from the source [20]. Thus, the MC approach is developed because it can give a better solution [21].

2.1.3.2 Monte Carlo method

The MC method based on stochastic numerical simulations of the RTE is used in this thesis to estimate the distribution of particles inside the medium. When the number of the observations increases, a more precise solution can be given by MC. So when the number of the observation is infinite, MC gives an exact solution. Although the number of the observation is limited in reality, MC still provides a precise solution, whereas with statistical noise. Therefore, the MC method is often considered as the gold standard to evaluate other approaches. The MC method provides a quite intuitive solution for tracing how the photons bounce inside the medium. Figure 2.5 shows a flow chart about how MC works. First, the photons are launched corresponding to the source including the photon position and its initial direction. Normally, a narrow collimated beam is incident perpendicularly to the medium surface, and the direction of the beam inside the medium is equally distributed with a solid angle over 4π.

The next step is to determine the step size that the photons move, which depends on μ_a and μ_s. The step size needed to reach the following scattering event is: $S_\mathrm{s} = -\frac{\ln(\xi)}{\mu_s}$, where ξ is just a random number and $\xi \in [0,1]$, while for the incoming absorption event is: $S_\mathrm{a} = -\frac{\ln(\xi)}{\mu_a}$. When $S_\mathrm{a} < S_\mathrm{s}$, the photon is absorbed before it reaches the next scatter. Otherwise, the photon is scattered first, the photons will change the direction in agreement with the scattering phase function $p(\hat{s}', \hat{s})$. The new direction is determined by the azimuthal angle, $\phi = 2\pi\xi$, and the deflection angle θ, $\cos\theta = \frac{1}{2g}(1 + g^2 - (\frac{1-g^2}{1-g+2g\xi}))$ derived from Eq.2.2. After being scattered into a new direction, the process continues. In the processes above, the most important is μ_a rather than the routines that the photons move. The Monte Carlo Multi-Layered (MCML) method was invented by Wang et al. [22] for biomedical applications. The simulations used in this thesis is MCML. When using the MCML method or the geometry of the medium is limited, the boundary conditions are considered. At the interface of different refractive indices n_i and n_t, the Fresnel reflection occurs. The averaged Fresnel reflection coefficient is given over the two different polarizations:

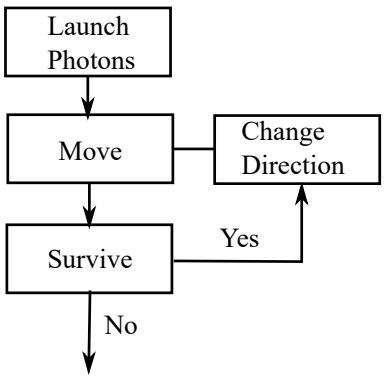

Figure 2.5: A flow chart of traditional Monte Carlo simulations, which trace only one photon each loop.

$$R(\theta_i) = \frac{1}{2}\left(\frac{\sin^2(\theta_i - \theta_t)}{\sin^2(\theta_i + \theta_t)} + \frac{\tan^2(\theta_i - \theta_t)}{\tan^2(\theta_i + \theta_t)}\right), \tag{2.7}$$

where θ_i is the incident angle and θ_t is the transmission angle, which can be obtained by using Snell's law, $n_i \sin\theta_i = n_t \sin\theta_t$. When the photons approach the boundary and the random number $\xi > R(\theta_i)$, the photons are transmitted, and their direction is determined by Snell's law. Whereas, if $\xi < R(\theta_i)$, the photons are reflected back to the original medium, and the processes move on.

However, when μ_a becomes larger, there are quite a lot of photons absorbed after moving a few steps, which means a large number of input photons are needed for MC simulations to predict a precise solution. So the implicit capture is introduced to reduce the number of the input photons in MC simulations, e.g., MCML. In this technique, packets of photons are launched and traced rather than one at a time. At first, an initial weight W_0 is allocated to each packet, then an average step size depends on the total attenuation coefficient, $\mu_{tot} = \mu_s + \mu_a$, after that, ΔW of the packet weight is decreased.

$$W_{i+1} = W_i - \Delta W = W_i(1 - \frac{\mu_a}{\mu_s}). \tag{2.8}$$

This process will end until the packets reach either the boundary of the medium or the threshold of the weight. If the packet weight is lower than the threshold and there is a probability of $1/m$ surviving, the process is terminated when there is no packet left. Otherwise, the weight of the packets is enhanced by m times [22].

White Monte Carlo (WMC) can be used for the time-resolved simulations, and it is used in the photon time-of-flight spectroscopy in this thesis. A database is run with a maximum scattering coefficient $\mu_s^{\max}$ and μ_a = 0. The photons are terminated when the time reaches the limit $t_{\max}$. μ_s can be obtained by scaling the temporal axis in infinite medium or semi-infinite medium. Normally, if the database is rescaled to a scattering coefficient $\mu_s = \mu_s^{\max}/\alpha$, then the time limit will extend to $\alpha t_{\max}$ as shown in Figure 2.6. Afterward, μ_a can be obtained by using Beer-Lambert law. Figure 2.7 illustrates how the WMC works using the implicit capture technique for the data evaluation. The maximal scattering coefficient $\mu_s^{\max}$, the time limit $t_{\max}$, and several parameters, e.g., g-factor, the numerical aperture (NA) of the fiber and refractive index of the phantoms are needed for the existing database. The database will be first rescaled according to the scattering coefficient range, the distance between two fibers (ρ) and fiber diameters (R_f) which are preset by users. Later on, the absorption coefficient is added according to the Beer-Lambert law. The WMC provides a scalable method for the time-resolved spectroscopy, and it is able to investigate a high absorption regime where the diffusion theory breaks down. This is due to the WMC simulation database is run with μ_a=0. Thus there is less need for a high albedo as compared to diffusion theory. Thence the simulation time is shortened due to a low albedo [21]. A specific spatial light source can be added by doing the convolution of MC simulations with the beam profile of the light source. The beam profile of the light source could be either Gaussian shape or top hat, and the beam diameter can be set arbitrarily. One more method has to be mentioned here is GPU-accelerated Monte Carlo, which is based on the identical theory, but using a parallel computation and leading to a 1000 times speedup. This method is used in this thesis. More detailed information can be found in [23, 24].

2.2 Slow light effect in a rare-earth ion doped crystals

2.2.1 Rare-earth ion doped crystals

The rare-earth elements (REE) contains 15 lanthanides, scandium, and yttrium. The electron configurations of REE are similar to the noble gas Xenon, whose 5s and 5p states are fulfilled. But an extra part $\mathbf{4f}^x\mathbf{5d}^y\mathbf{6s}^2$ is added, where x is between 0-14 starting from Lanthanum (La) to Lutetium (Lu), and y is 1 for Lanthanum (La), Cerium (Ce) and Gadolinium (Gd), while 0 for the rest. The REE are usually triply ionized when doped into crystals. This is achieved by the delocalization of

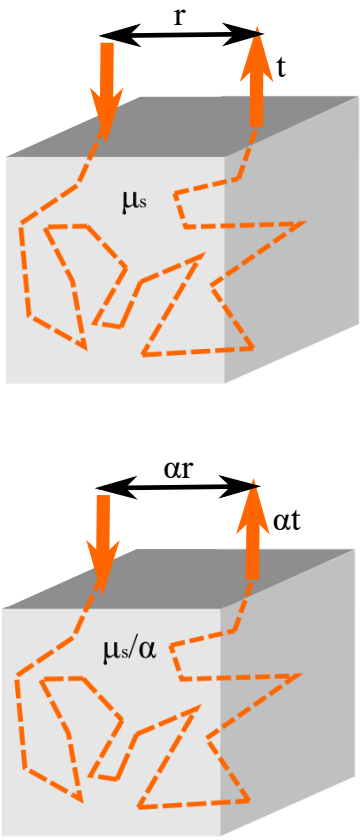

Figure 2.6: The paths are created in a media with μ_a=0, and it can be rescaled for different scattering coefficient μ_s. This is because only the phase scattering function determines the propagation direction of the light in WMC simulation.

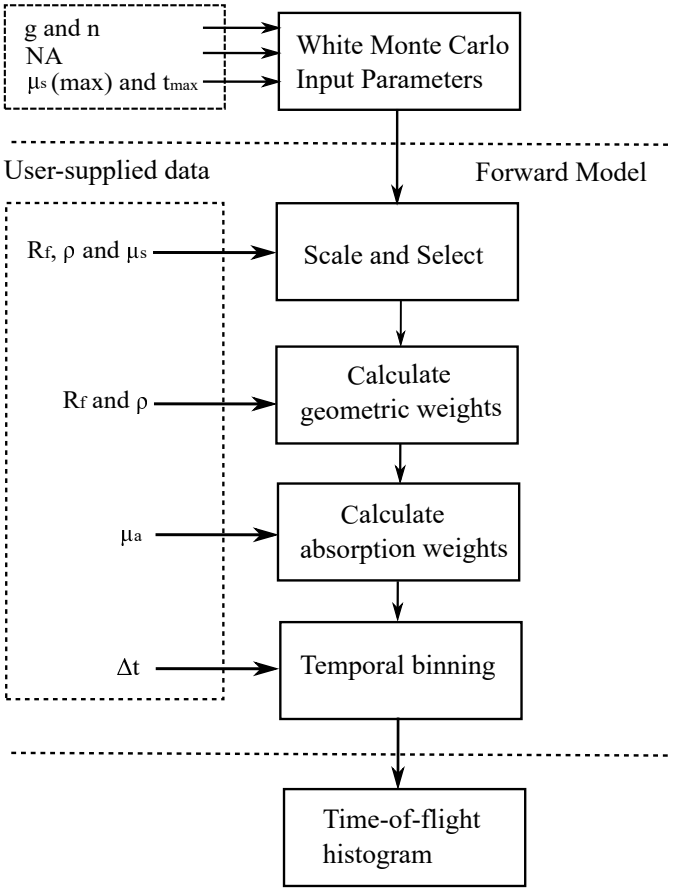

Figure 2.7: The WMC database is obtained after the input parameters anisotropic factor g and refractive index n of the material, the numerical aperture of fiber NA, and the range of the database t_{max} and μ_s^{max}. The forward model is used to rescale the database and generate time-of-flight histogram by using the parameters: the radius of the optical fiber R_f, the source-detector separation ρ, the material properties μ_s' and μ_a. and the temporal channel width Δt, figure cited from [21].

two electrons in the 6s subshell and one electron in the 5d subshell or 4f subshell when there is no electron in the 5d subshell from the nucleus. Therefore, the trivalent RE ions (RE^{3+}) have 0-14 valence electrons in the 4f subshell. The RE^{3+} ions, when doped into crystals, can be considered as free atoms since the electrons in the 4f subshell are protected by the fully filled outer-lying 5s and 5p subshells. When the RE^{3+} ions are doped into non-centrosymmetric crystals, forbidden transitions, e.g. 4f-4f transitions are weakly allowed. Due to these, the RE ions possess remarkable properties of long coherence time and lifetime of hyperfine levels, which are favorable for creating a slow light spectral filter. A cryostat is required to reduce phonon-electron interactions. The phonon-electron interactions cause decoherence, and the decoherence is proportional to T^7 [25, 26]. In this thesis, praseodymium (Pr) doped in a yttrium orthosilicate (Y_2SiO_5) crystal is used for creating a slow light spectral filter. For trivalent praseodymium (Pr^{3+}), there are two electrons in the 4f subshell. The fine structure levels can be presented by $^{2S+1}L_J$, where J is the total angular momentum obtained from the coupling of the total electron spin (S= 0 or 1) and the total orbital angular momentum (L= 0,1,2...6). The transition $^3H_4 \rightarrow {}^1D_2$ (605.977 nm) is used for Pr^{3+}:Y_2SiO_5. The hyperfine levels are induced by the interaction of the nuclear spin (I= 5/2) of the Pr ion (only one isotope,

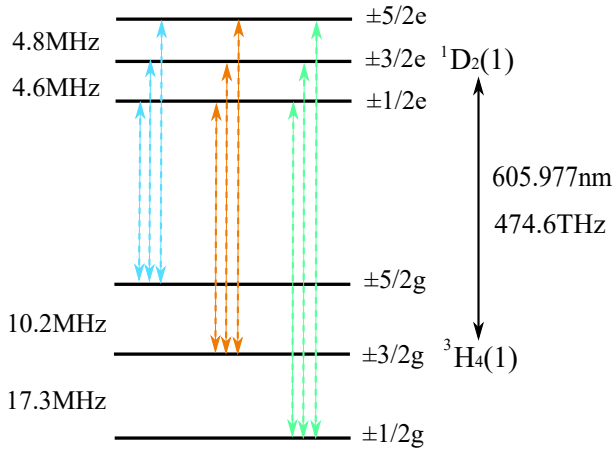

Figure 2.8: The energy structure of 0.02% Pr^{3+}:Y_2SiO_5 under 1.4 K at *site I*[27, 28], and the transitions are presented by arrows.

^{141}Pr) and the total electron angular momentum (J). The first-order hyperfine interactions are faded away since Pr^{3+} with an even number of 4f electrons has electronic singlet levels and the total angular momentum is quenched by the crystal field [29]. Nonetheless, the hyperfine levels of Pr^{3+} are mainly caused by the second-order interactions which are related to the square of nuclear spin [30], thus the hyperfine levels doubly degenerate into m_I=± 5/2, ± 3/2 and ± 1/2 with nuclear magnetic quantum numbers at a zero magnetic field as shown in Figure 2.8.

The host crystal yttrium orthosilicate (Y_2SiO_5) is considered as a popular host thanks to its attractive properties, for example, the low nuclear magnetic moments and that it can be grown as a bulk crystal. More detailed information is given in Appendix B.

2.2.2 Persistent spectral hole-burning

The properties of spectral broadening of Pr^{3+}:Y_2SiO_5, which affect the absorption profiles of atoms, is of importance for spectral hole-burning. Since the homogeneous absorption linewidth of individual ions is considerably narrower than the inhomogeneous linewidth at 4 K, this makes it possible only to excite the ions at a small laser frequency range.

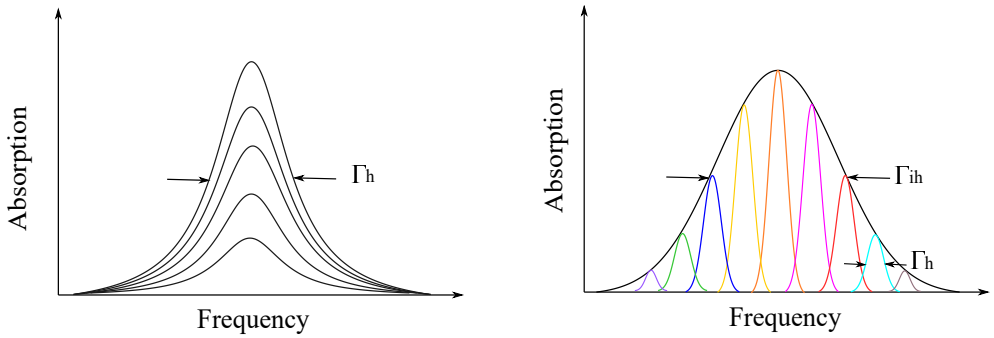

Figure 2.9: Left is the homogeneous lineshape with homogeneous linewidth Γ_h, and the inhomogeneous linewidth Γ_{ih} on the right part is the sum of all individual homogeneous linewidth Γ_h.

The **homogeneous linewidth**, Γ_h, is inherent characteristic in all the transitions, which affects all the ions in the same way. Homogeneous linewidth comes from two mechanisms, one is the lifetime of the excited state (T_1), the other is the relaxation time of the excited state (T_2^*), referred as dephasing process, which doesn't affect the lifetime, but the transition frequencies. Moreover, the

linewidth is the spectral width of the absorption profiles of individual ions, which has a Lorentzian line shape as shown in Figure 2.9 (left). This can be related to the coherence time (T_2) through the Fourier transform. Therefore, there is a summarized relation between the homogeneous linewidth, Γ_h, the excited lifetime T_1, the relaxation time T_2^* and the coherence time T_2:

$$\Gamma_h = \frac{1}{\pi T_2} = \frac{1}{2\pi T_1} + \frac{1}{\pi T_2^*}. \tag{2.9}$$

From this relation, we can see that the optimal condition is when there are no other broadening processes that contribute to the decoherence except the lifetime decay of the excited state, that means T_2=2T_1. This also shows the coherence time is confined by the finite lifetime. Furthermore, the narrower the homogeneous linewidth is, the longer coherence time can be obtained. The narrow, homogeneous linewidth is attractive for the spectral hole burning, which makes it possible to drive a group of ions by a particular laser frequency range. More discussion about the coherence time is shown in Appendix C.

The **inhomogeneous linewidth**, Γ_{ih}, comes from that the ions are embedded in a slightly different crystal environment. This means transition frequencies of individual ions are slightly different as shown in Figure 2.9 (right). The distinctness could be caused by the different crystallographic sites, isotopes of the host ions and vacancies, etc. [31] Adding the homogeneous broadening of individual ions contributes to an inhomogeneous broadening with a fairly wide Gaussian-shaped linewidth. The inhomogeneous linewidth, Γ_{ih}, normally has an order of several GHz as compared to the homogeneous linewidth, Γ_h, typically with an order of a few kHz for the low doped concentration Pr^{3+}:Y_2SiO_5 crystal at cryogenic temperature.

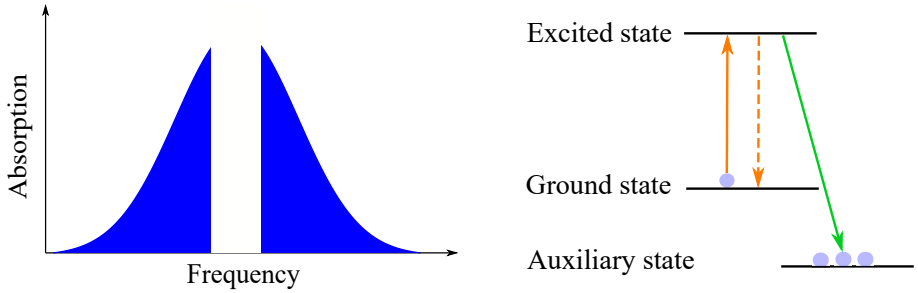

Figure 2.10: A spectral hole is created when the excited ions decay back to the auxiliary state rather than the initial ground state. Auxiliary state is referred to the other hyperfine levels in the ground state. Left shows an spectral hole in the frequency domain, while a simplified configuration is on the right part.

The spectral filter is created by using the spectral hole-burning technique. From the discussion above, the inhomogeneous linewidth is much wider than the homogeneous linewidth. When the laser light propagates through the crystal, a small fraction of ions within the inhomogeneous linewidth will be excited, providing that the laser linewidth is significantly narrower than the inhomogeneous linewidth. This small fraction excited ions form a transient hole since the absorption of the original ground state where they were excited is reduced, and it will last for the lifetime of the excited state. If part of the excited ions will relax to the other hyperfine levels of the ground state rather than the original ground state, such a hole will be considered as persistent as shown in Figure 2.10. This is due to the lifetime of the ground state is typically longer than that of the excited state. The hyperfine levels of ground state lifetime are around several seconds of Pr^{3+}:Y_2SiO_5, and it could be extended to a few minutes by adding a small magnetic field. However, not only the main spectral hole will be created, but also *side-holes* as well as *anti-holes* will appear. The side-holes will occur

when the ions in the same ground state are transferred to the other hyperfine levels in the excited states. The anti-holes are shown up with increased absorption when the ions that were moved to new the hyperfine levels of the ground state are excited. The actual condition is more complicated as a result of the inhomogeneous broadening. Different groups of ions could be resonant with the same optical frequency but experience different transition frequencies as shown in Figure 2.11.

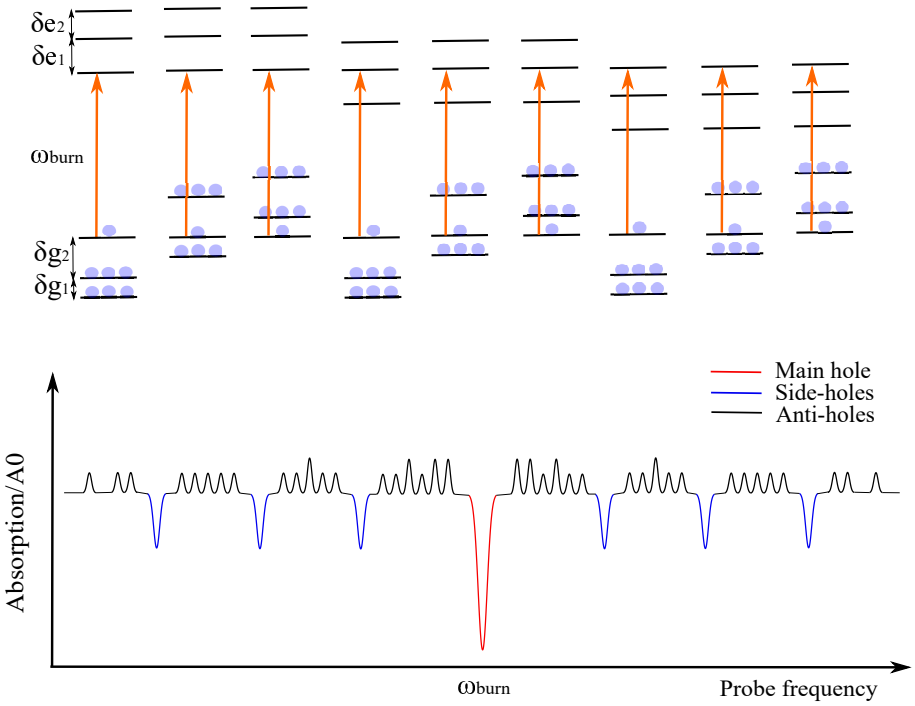

Figure 2.11: One laser frequency can drive 9 different transitions due to the interaction with different group of ions (Above). The side-holes and anti-holes are generated during the spectral hole burning process (Below). Adapted from [30].

2.2.3 Slow light filter

When light propagates through a narrow spectral hole within a highly absorbing frequency region, the frequency dependent refractive index in the vicinity of the spectral hole is shown in Figure 2.12. The speed of the overall envelope of the wave is called the group velocity, $\upsilon_g(w)$, and it can be expressed as:

$$\upsilon_g(w) = \frac{\partial w(k)}{\partial k} = \frac{c_0}{n(w) + w\frac{\partial n(w)}{\partial w}}. \tag{2.10}$$

Due to the sharp refractive index dispersion curve inside the spectral hole ($w\frac{\partial n(w)}{\partial w} \gg n$), the group velocity is slower than the speed of light, which is called the slow light effect, and in the region where the group velocity is faster than the speed of light, this is addressed as the fast light effect. The slow light effect is similar to the way that electrical pulses are delayed when passing through a band-pass filter in the circuits. The slowed down light velocity can be approximately determined by $\upsilon_g(w) \approx 2\pi\Gamma/\alpha$ [32], where α is the absorption coefficient outside the hole, and Γ is the linewidth of the spectral hole. Thus, the narrower the spectral hole is, or the higher absorption outside the hole is, the light will be slowed down more significantly. As discussed above, the linewidth of the spectral hole depends on both the homogeneous linewidth and laser linewidth. So a thin homogeneous linewidth and laser linewidth are required to achieve a considerable slow light effect.

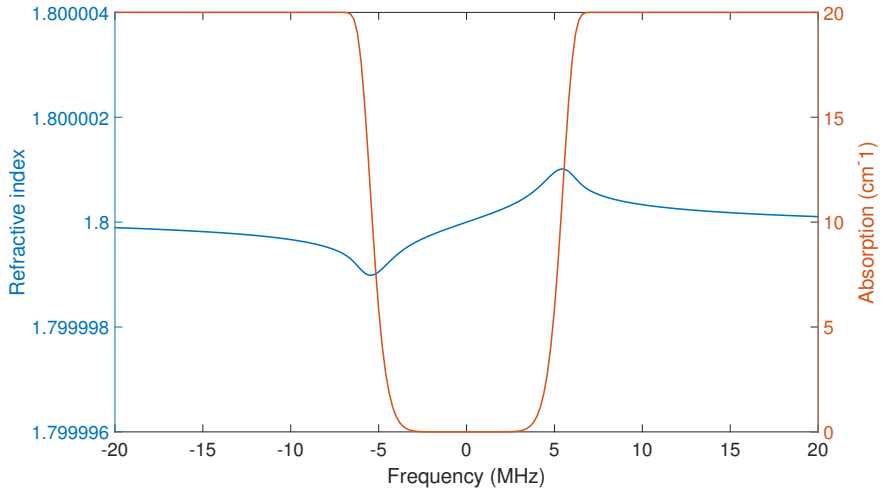

Figure 2.12: A strong normal dispersion inside the spectral hole

2.3 Coherent light-matter interaction

The optical Bloch equations are used to represent a two-level atomic system quantum mechanically when interacting with the coherent laser light field, where the external field is described by the Maxwell wave equations classically. Therefore, the coherent light-matter interaction process in this thesis is illustrated by using this simplified semi-classical approach.

2.3.1 The Bloch Sphere

To describe a two-level open system from a view of quantum mechanics, two phenomenological decay constants T_1 and T_2 are introduced by M.O. Scully et al. [33] to the time-dependent density matrix, where T_1 and T_2 are the lifetime and decoherence time of the excited state respectively, and the inversion of them are the decay rate and decoherence rate. So the derivative of Bloch equations based on the Bloch vector, after considering the rotating wave approximation [33], is expressed as:

$$\frac{dr_x}{dt} = -\frac{1}{T_2}r_x - \Delta r_y + \Omega_i r_z, \tag{2.11}$$

$$\frac{dr_y}{dt} = \Delta r_x - \frac{1}{T_2}r_y + \Omega_r r_z, \tag{2.12}$$

$$\frac{dr_z}{dt} = -\Omega_i r_x - \Omega_r r_y - \frac{1}{T_1}(r_z + 1), \tag{2.13}$$

where r_x, r_y and r_z are the Bloch vector components, and the benefit of using them is to give an intuitive picture which will be discussed below. Δ= ω_0-ω_L is the detuning frequency which represents the difference between the resonance frequency and the laser frequency. The Rabi frequency Ω are used to depict the relative oscillation strength between the atom and the coherent laser light field as below:

$$\Omega_{i\to j} = \frac{\overrightarrow{\mu}_{i\to j} \cdot \overrightarrow{E}(z,t)}{\hbar} e^{i\psi(t)}, \tag{2.14}$$

where i and j are the initial ground state and the final excited state, E is the amplitude of the electric field, and the phase information is given by ψ, and μ is the transition dipole moment between the

ground state and the excited state ($\overrightarrow{\mu}_{g\to e} = -e\langle g \mid \overrightarrow{r} \mid e\rangle$), $\hbar$ is the Planck constant. Ω_r is the real part of the complex Rabi frequency which gives the laser pulse shape, while Ω_i is the imaginary part which contains information on the frequency change during the pulse.

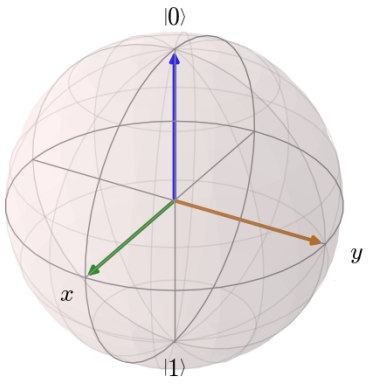

Figure 2.13: A Bloch sphere is used to represent any Bloch vectors. The blue arrow represents the ground state, the green arrow and the brown arrow provides a superposition state of the ground and the excited state. Cited from [34].

Since the state of the atom is a coherent superposition of the ground state and the excited state for a two-level system, it can be expressed with the help of the Bloch vectors which can be pictured by the Bloch sphere. Hence an arbitrary state of the atom can be given:

$$\mid \Phi\rangle = c_0(t) \mid 0\rangle + c_1(t)e^{-i\omega_0 t} \mid 1\rangle, \tag{2.15}$$

$$\mid c_0(t) \mid^2 + \mid c_1(t) \mid^2 = 1, \tag{2.16}$$

where $\mid c_0(t) \mid^2$ and $\mid c_1(t) \mid^2$ are the normalized probabilities of the ground state and the excited state, which are represented by $\mid 0\rangle$ and $\mid 1\rangle$ respectively. ω_0 is the angular resonance frequency between the ground state and the excited state. A more convenient way is to use the Bloch vectors to describe the atom state of a two-level system. Thus the Bloch vectors are given corresponding to the probability amplitudes:

$$r_x(t) - ir_y(t) = 2 \cdot c_0 \cdot c_1^*, \tag{2.17}$$

$$r_z = \mid c_1(t) \mid^2 - \mid c_0(t) \mid^2, \tag{2.18}$$

where r_x and r_y in the equatorial plane give the phase information which describes the oscillation coherence of the atomic transition, and r_z represents the difference between the atom probabilities of staying in the excited state and that of remaining in the ground state. These Bloch vectors can be depicted in terms of the angle θ and ϕ in the Bloch sphere as shown in Figure 2.13. Therefore, the state of the atom can be expressed with the help of the Bloch sphere:

$$\mid \Phi\rangle = e^{i\psi} \sin\frac{\theta}{2} \mid 0\rangle + \cos\frac{\theta}{2} \mid 1\rangle. \tag{2.19}$$

Through this intuitive graph, vectors are used to visualize the atom state. The ground state is when the vector straightly points down, while the excited state is presented when the vector straightly points up. Actually, all positions existing in the Bloch sphere correspond to different states when considering the relaxation and dephasing process in this model.

2.3.2 The Maxwell-Bloch Equation

A simulation based on Maxwell-Bloch equations can be used to take the light polarization and tapering light intensity along the thickness of crystal into account. As mentioned above, the Bloch equations describe the quantized atomic system, while the Maxwell wave equations describe the classical external field. Therefore, together with the Maxwell wave equations, the numerical simulation of the Maxwell-Bloch equations are derived by Thuresson [35] as follow:

$$\frac{dr_x(z',\tau,\Delta)}{d\tau} = -\Delta r_y(z',\tau,\Delta) - \Omega_i(z',\tau) r_z(z',\tau,\Delta) - \frac{r_x(z',\tau,\Delta)}{\mathrm{T}_2}, \tag{2.20}$$

$$\frac{dr_y(z',\tau,\Delta)}{d\tau} = \Delta r_x(z',\tau,\Delta) - \Omega_r(z',\tau) r_z(z',\tau,\Delta) - \frac{r_y(z',\tau,\Delta)}{\mathrm{T}_2}, \tag{2.21}$$

$$\frac{dr_z(z',\tau,\Delta)}{d\tau} = \Omega_i(z',\tau) r_x(z',\tau,\Delta) - \Omega_r(z',\tau) r_y(z',\tau,\Delta) - \frac{1 + r_z(z',\tau,\Delta)}{\mathrm{T}_1}, \tag{2.22}$$

$$\frac{d\Omega_r(z',\tau)}{dz'} = \frac{\alpha_0}{2\pi} \int_{-\infty}^{\infty} g(\Delta) r_y(z',\tau,\Delta) d\Delta, \tag{2.23}$$

$$\frac{d\Omega_i(z',\tau)}{dz'} = -\frac{\alpha_0}{2\pi} \int_{-\infty}^{\infty} g(\Delta) r_x(z',\tau,\Delta) d\Delta, \tag{2.24}$$

where $\tau(z,t) = t - \frac{z'n}{t}$ is the retarded time due to the slow light effect, and z is the thickness of the crystal which is divided into 101 slices in the simulation. z' is defined as $z'(z,t) = z$ for convenience. $g(\Delta)$ is the profile of inhomogeneous broadening, and α_0 is a relative absorption coefficient which can be defined as $\alpha_0 = \alpha_(w_0)/g(w_0)$, and w_0 is the resonance frequency of the atomic transition. More derivation details are provided by the Thuresson's master thesis [35]. This numerical simulation considers the effect caused by the thickness of the crystal and the polarization direction of the incoming laser light, and it consists of three nested loops. The outer loop is the thickness of the crystal (z'), then the middle part is the detuning frequency (Δ), and the inner loop runs over the Bloch equations which are solved by 4th order Runge-Kutta for each Δ and z'. The last part is an integral part as shown in Eq.(2.23) and Eq.(2.24) for the Maxwell functions describing the back action of the ions on the electromagnetic field by considering the atomic polarization and the propagating laser light.

2.4 Simulations

2.4.1 Monte Carlo

For the Monte Carlo simulation, a phantom has to be defined with refractive index, absorption coefficient, scattering coefficient, g-factor and the thickness of the phantom. A large number of photons is used to mimic the light propagation inside the phantom. Several layers with the different refractive index can also be added. A Gaussian shape or top hat light source can be implemented by using convolution, where the power and beam radius can be set. The fluence distribution of a phantom with n= 1.33, μ_s'= 23.34 cm^{-1}, μ_a= 0.01 cm^{-1}, g= 0.7 and d= 10 cm, and using one billion photons, is shown in Figure 2.14. Additional information such as reflection, absorption and transmission as a function of radius (r), depth (z), angle (a) and layer (l) can be derived from fluence distribution, and the output angle can be found on the surface of the phantom. Therefore, the Monte Carlo simulation can be used to calculate how much light is transmitted through the phantom or the light intensity impinging on any specified area.

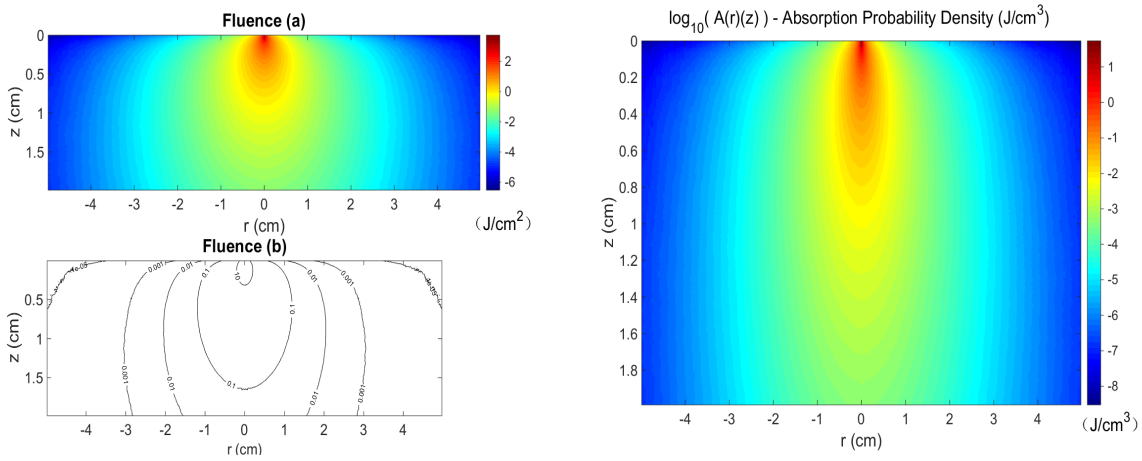

Figure 2.14: The fluence distribution of a phantom with (right), and the absorption probability per area can be derived from the fluence distribution (left).

2.4.2 Spectral hole burning

Table 2.1: Rabi frequency for P=20 mW, w_0 is 10 mm along D_2 polarization

Rabi frequency (g/e)	1/2	3/2	5/2
1/2	20.0 kHz	14.3 kHz	5.7 kHz
3/2	14.3 kHz	22.8 kHz	2.9 kHz
5/2	5.7 kHz	4.3 kHz	25.7 kHz

A Bloch simulator based on Bloch equations is used to optimize the parameters of the pump pulses to burn a spectral hole more efficiently. However, the Bloch simulator only considers a two-level system. It is only necessary to consider the lifetime decay (T1) and the decoherence time (T2) of the excited state. As mentioned in Figure 2.11, one laser frequency will be resonant with nine different groups of ions. These nine transitions have different transition strengths. The Rabi frequency for different transition when I= 250 W/cm^2 is given in [28]. For the simulation of the actual hole-burning experiment, 20 mW for the laser power is a reasonable choice. Hence, the Rabi frequencies of polarization along D2, which is discussed in Appendix B, corresponding to different transitions under the assumption of 20 mW laser power and 10 mm beam diameter are shown in Table 2.1. Thence the Rabi frequency of polarization along D1 can be inferred from Figure B.1.

The *sechyp* pulse was used in the simulation in order to burn the ions more efficiently. A complex *sechyp* pulse contains two parts. The real part gives the pulse shape as shown in Figure 2.15, while the imaginary part can be considered as a frequency scan in the time domain as given in Figure 2.16.

The height of the pump pulses for creating the spectral hole corresponds to the amplitude of the Rabi frequency, the FWHM of the pulse (t_{FWHM}) correlates to the edge of the pulse, and pulse duration t_{cutoff} is the length of the pulse in Figure 2.15. The frequency scan (f_{scan}) relates to the flat top of the pulse in Figure 2.15. Moreover, the width of the pulse (f_{width}), also referred to inversion region width, corresponds to the frequency span shown in Figure 2.16. The population of the excited state as predicted by the Bloch equation simulation and the optimized parameters are shown in Figure 2.17. The Rabi frequencies used in the Bloch simulator are shown in Table 2.1. Different Rabi frequency gives different population.

The maximum population of nine transitions can be put in a hole burning simulation since this simulation has considered the decay from the excited state. It also considers different oscillation

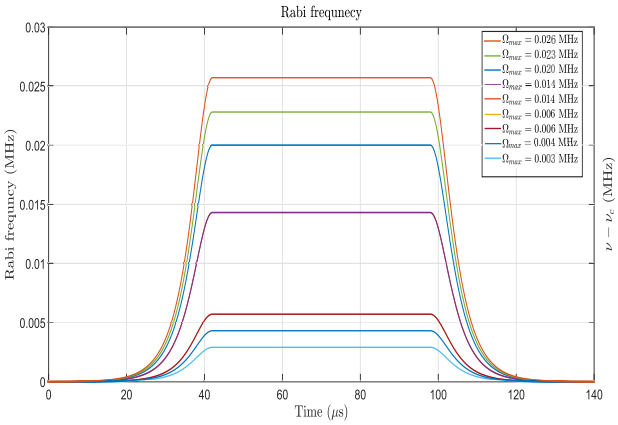

Figure 2.15: The pulse shape for different Rabi frequency, which comes from the real part of the Rabi frequency.

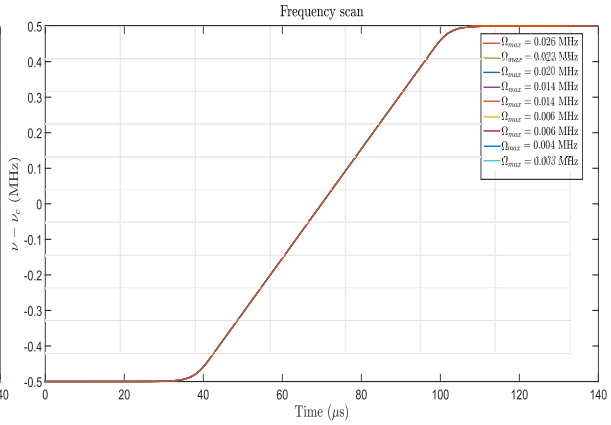

Figure 2.16: The frequency scan for different Rabi frequency, and it is the imaginary part of the Rabi frequency.

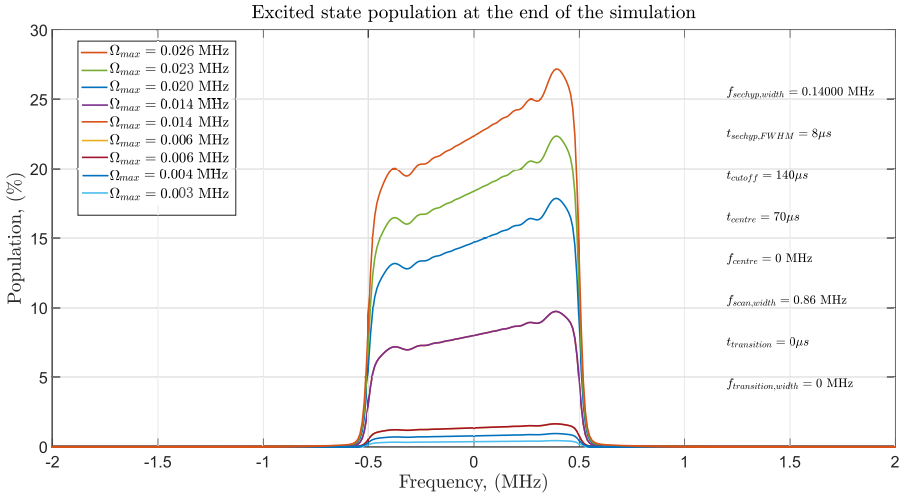

Figure 2.17: The population of the excited state for nine transitions at the end of the simulation. The optimized parameters is shown on the left part of the figure.

strength of 9 transitions in Table 2.1. The transmission in the far away as shown in 2.18 is around $5 \cdot 10^{-8}$ since the absorption coefficient of the D2 axis is around 20 cm^{-1}, more discussion is in section 3.3. Thus this simulation gives more accurate result compared to only consider a two-level system. The suppression of the transmission between the center of the spectral hole and 1.5 MHz away is shown in Figure 2.18. The number of the pump pulses can be inferred from the simulation with the highest suppression ratio. However, more losses come from the cryostat in real conditions, and this simulation doesn't give the structure information of the spectral hole.

One more simulation is used to give the structure of the spectral hole, and the spectral hole structure along the thickness of the crystal based on the Maxwell-Bloch equations. Several tests of different polarization and minor changes in the pulse parameters are shown in Figure 2.19, 2.20, which provides different pulse shape and frequency sweep corresponding to the changes. The spectral hole structure is given in Figure 4.4, and it is better to burn along D2 polarization. The sawtooth inside the spectral hole comes from the limitation of the simulation. In the real experiments, it doesn't exist.

Due to the thickness of the crystal, the laser pulse will be absorbed strongly in the front surface of

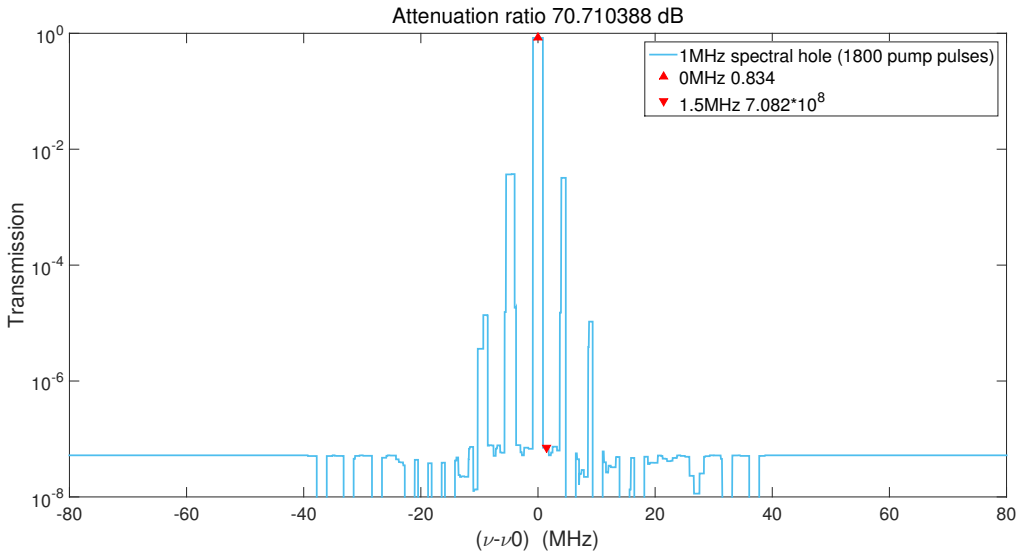

Figure 2.18: Suppression between the center of the spectral hole and 1.5 MHz away is used to simulate the number of the pump pulses.

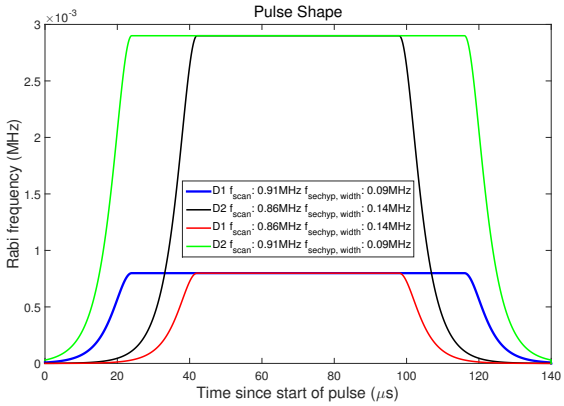

Figure 2.19: The pulse shape changes with different frequency scan, pulse width, and the polarization.

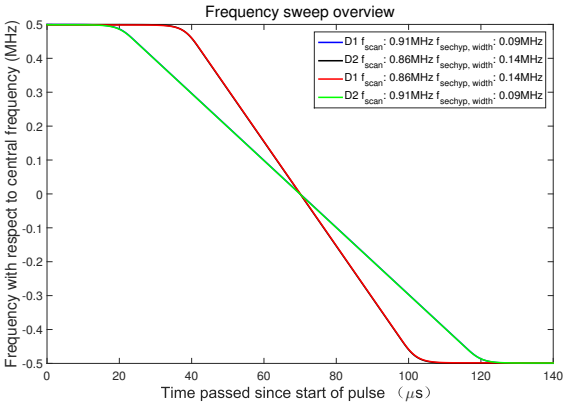

Figure 2.20: The frequency sweep changes with different frequency scan, pulse width, and the polarization.

the crystal, but less laser power for the next surface. Then next laser pulse will be strongly absorbed in a deeper position and goes on. So the spectral hole out of the crystal might be different from the one burned at the beginning of the crystal, thence we used different optimized parameters to see to what extent the spectral hole suffers this problem. This problem is not evident for four groups of the optimized parameters. As shown in Figure 2.22, the spectral hole is quite even along the thickness of the crystal from one of the four groups of the optimized parameters.

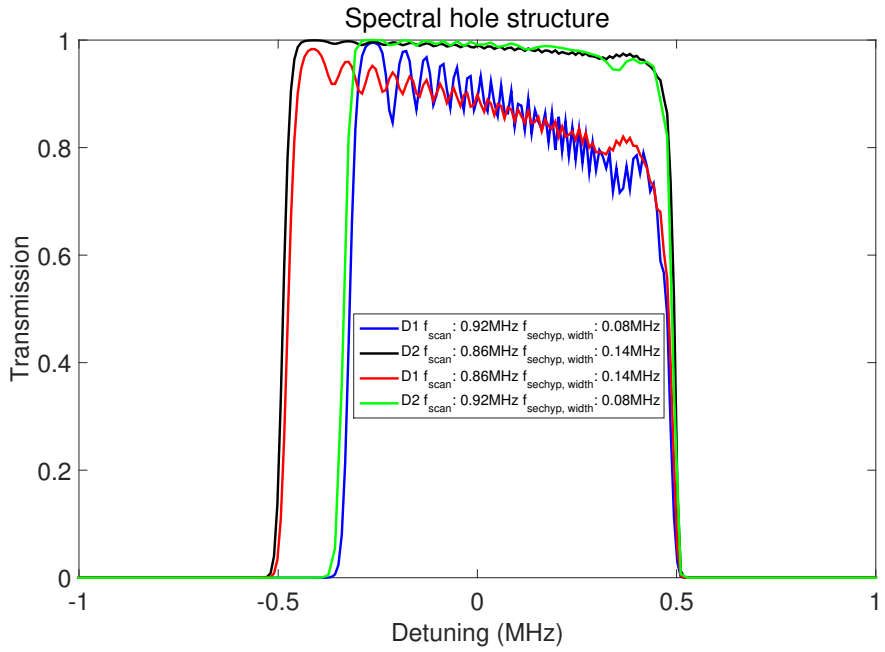

Figure 2.21: The spectral hole structure changes with different frequency scan, pulse width, and the polarization. The black line gives a better hole.

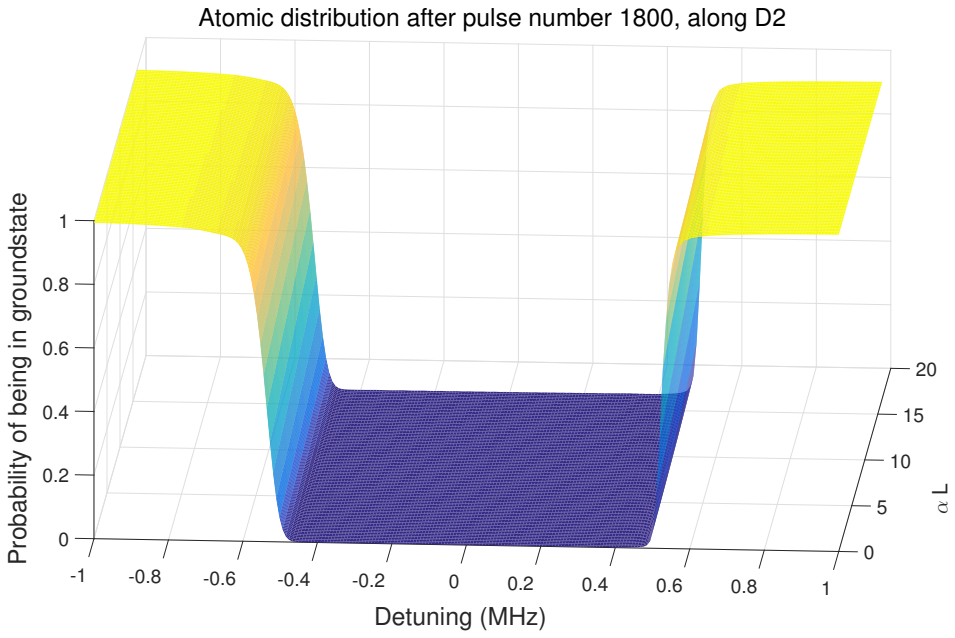

Figure 2.22: The spectral hole structure along the thickness of the crystal.

Chapter 3

Experiments

3.1 Absorption spectroscopy

The phantoms are used to mimic the scattering coefficient and absorption coefficient of the human tissue. In this section, the absorption coefficient can be measured by direct absorption spectroscopy. Meanwhile, this method validates the photon time-of-flight spectroscopy which can be used to measure both the scattering coefficient and absorption coefficient. Therefore, the absorption coefficient and the scattering coefficient of the phantoms could be entirely controlled by using these two methods.

3.1.1 Direct absorption spectroscopy

3.1.1.1 Preparation of phantoms

The liquid phantoms, with different absorption coefficients, are made for the direct absorption spectroscopy. First, the Indian ink (Royal Talens) diluted with distilled water was used to make ink bases with a ratio of 1:100. Then a bottle of diluted ink was put inside the ultrasonic cleaner (Branson B1200R-4) which was filled with deionized water, for 2h. The ultrasonic cleaner was to disintegrate the ink particles and make their size as homogeneous as possible. However, the ink base has a limited lifetime due to sedimentation. Afterward, the magnetic stirrer (SKAFTE Medlab) was used for mixing them for 1h. Three series of different ink concentration made of ink base (1:100) were used in the experiment as shown in Table 3.1 and each series contained ten samples with different concentrations of ink base (1:100) dissolved in the different amount of distilled water, while keeping the total volume to 3ml. Three series correspond to three different groups of measurements using different ink concentration as shown in 4.1.

Table 3.1: Three series of different concentration using ink base (1:100). Series 1 corresponds to sample 1, series 2 matches sample 2,3 and 4, and series 3 is the concentration of sample 5 and 6.

Sample number	000	001	002	003	004	005	006	007	008	009
Series 1 ink base concentration (%)	0	0.5	0.83	1.17	1.5	1.83	2.16	2.5	2.92	3.17
Series 2 ink base concentration (%)	0	0.25	0.42	0.58	0.75	0.92	1.08	1.25	1.46	1.58
Series 3 ink base concentration (%)	0	0.025	0.05	0.075	0.1	0.125	0.15	0.175	0.2	0.225

These samples were contained in ten $10 \times 10 \times 35$ mm cuvettes which are made in optical polystyrene. These cuvettes can be used for the most polar solvents, acids and alkaline solutions with the wavelength range from 300 nm to 900 nm [36].

3.1.1.2 Measurements

The experimental setup of direct absorption spectroscopy is depicted in Figure 3.1. A Tungsten Halogen Light Source (HL-2000-FHSA) with Attenuator and TTL-shutter emitted the light from 360 nm to 2400 nm, which has the output power of 7 W. Moreover, this type of light source included a connector (SMA 905) to efficiently couple light into the fiber [37]. A cooling fan was attached at the bottom of the light source. The light source needed more than 10 minutes to warm up and five more minutes to stabilize. A multi-mode fiber (Thorlabs M41L02) with a diameter of 600 μm was used to guide the light into the Temperature Controlled Cuvette Holders (Ocean Optics QPOD 2e), where the temperature could be adjustable between $-30°$C and $+105°$C with a precision and accuracy of $\pm 0.01°$C and $\pm 0.15°$C respectively [38]. The temperature was set at 20°C by the software Q-Blue. The cuvettes sat in the middle of the holder and two attenuation slits were placed at two sides of the cuvettes with different size (one is 4 mm, the other is 2 mm) in order to simulate a collimated light. In addition, two collimated lens system with SMA connectors were included to maximize the light coupling into a fiber. Afterward, the light was split into two parts (50% each) by a fiber splitter and detected by two spectrometers. One is visible spectrometer (Ocean Optics QE65000) with the spectral range 200-1100 nm, a bandwidth of 6 nm, and the integration time from 8 ms to 15 min [39], the other one is NIR spectrometer (Ocean Optics NIRQuest512) with wavelength range 900-1700 nm, a bandwidth of 3 nm, and integration time 1 ms-120 s [40].

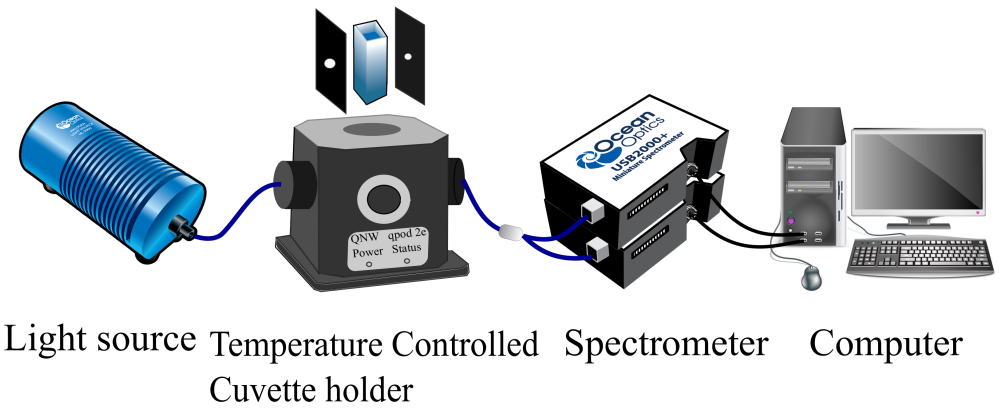

Figure 3.1: Schemetic diagram of the direct absorption spectroscopy. The blue line presents fiber and the black line states electrical cable.

When doing the measurements, the integration time of both spectrometers was needed to be set manually in case of saturation. Thus the integration time of the visible spectrometer is 9 ms which is better to set it a little bit higher than the limit (8 ms), while that of the infrared one is around 10 s. The number of scans was also set differently due to different integration time, ten scans for visible spectrometer as compared to one scan for the NIR spectrometer. Afterward, the reference sample with 3 ml of distilled water was put in the holder, and the background and reference spectrum were recorded when closing and opening the shutter of the light source respectively. Actually, the obtained spectrum of the samples as mentioned in Table 3.1 were transmission spectrum. At last, the absorption coefficient could be calculated from Equ. 2.6.

3.1.2 Photon time-of-flight spectroscopy

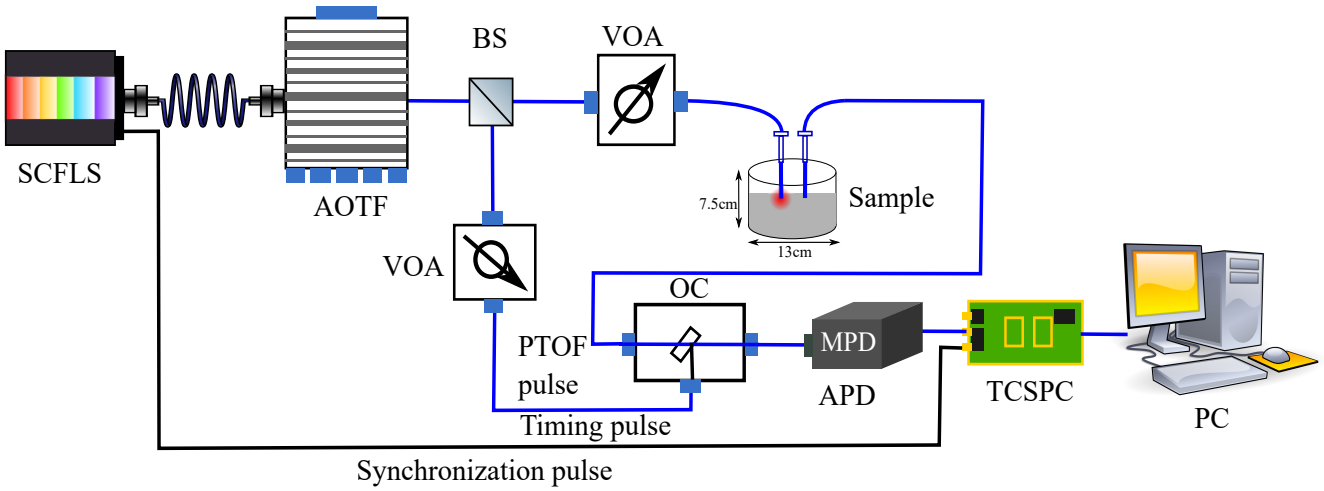

Figure 3.2: Schematic diagram of photon time-of-flight spectroscopy. SPCFLS: Super continuum fiber laser source, AOTF: Acousto-optic tunable filter, BS:Beam splitter, VOA:Variable optical attenuator, OC:Optical combiner, APD: Avalanche photon detector, TCSPC: Time-correlated single photon counting, PC: Personal computer. The blue line denotes fiber and the black line states electrical cable.

Three types of phantoms were made for the Photon Time-Of-Flight spectroscopy (PTOF). For this system, adding scatterers is a must. Thus 5 ml, 10 ml, and 15 ml Intralipid 20% (Fresenius Kabi AB, Uppsala) mixed with 395 ml, 390 ml, and 585 ml distilled water respectively. The diluted ink from the same ink base (1:100) was added varying from 0 ml to 2.5 ml. The experimental setup of PTOF system is shown in Figure 3.2. The Super Continuum Fiber Laser Source (SCFLS: Fianium SC500-6) provides a broadband light from 500-1850 nm with a 6 W output power. Its master source has a repetition rate of 80 MHz and generates 6.0 ps pulses. A narrow band pulse at a specific wavelength could be selected after passing through the Acousto-Optical Tunable Filters (AOTF: Fianium 10-1571). This can be achieved by exposing a birefringent crystal to an acoustic wave which is generated by a transducer. The AOTF has two output ports: one is visible from 400-690 nm with a bandwidth of 2-4 nm, the other is NIR from 650 nm to 1000 nm with a bandwidth of 4-6 nm. The light was guided by a graded-index fiber (GRIN) whose core diameter is 400 μm, and the cladding is 600 μm, into a beam splitter. 96% of the light was transmitted and led to phantoms, while 4% was reflected as a reference. Two attenuators with a range from -2.68 dB to -40 dB were used in each path to adjust the light intensity since the Time-Correlated Single Photon Counting (TCSPC) card needs to detect a single photon or no photon in the beam path, and the medical safety limitation also need to be considered. The phantoms were put in a cylinder container whose size is 11 cm$\times$11 cm$\times$7.5 cm. Then the source fiber and the detecting fiber were placed in parallel with a separation of 20 mm, and perpendicular to the phantom surface with a depth of 10 mm. Afterward, the PTOF signal and the reference signal were combined by an optical combiner and sent to a single-photon avalanche photodiode (SPAD: PDM100ct). The electric output of the SPAD was delivered to a Constant Fraction Discriminator (CFD) which is used to avoid the amplitude fluctuations of the signals. A synchronization pulse was sent out directly from the SCFLS to another CFD. The output pulses of the CFDs were transferred to a Time to Amplitude Converter (TAC) to start and stop the internal clock. It should be mentioned that the detector signal starts the clock and the synchronization pulse stops it. Then the time delay between signals could be converted into a voltage using TAC. At last, the different voltages of accumulated photons were

analyzed by a Multi-Channel Analyzer (MCA) to obtain a histogram of photon distribution versus time channels (the arrival time of each detected photon). The technique mentioned above is called the Time-Correlated Single Photon Counting (TCSPC) which is based on a TCSPC card.

When doing the measurements, at first, an Instrumental Response Function (IRF) was measured by using a double printed black paper inside a tablet holder. It tested the time delay of the whole system including electronics. Then the IRF was convoluted with the theoretically modeled pulse to fit experimental data. 25 groups of data were collected for each measurement. For the data evaluation, White Monte Carlo was used to obtain the scattering coefficient and absorption coefficient.

3.2 Transmitted light as a function of scattering and absorption

The experiment is to measure how much light can be detected on the surface of phantoms and whether it matches with the simulation, and the goal for this is to be aware of how much light is transmitted through the ultrasound focus from the simulation in the future.
The experimental setup is shown in Figure 3.3. A laser diode (Thorlabs CPS180) with a wavelength of 635 nm and an output power of 1 mW was used. Then the light was guided by a fiber with a diameter of 600 μm. A convex lens in a lens tube was put between the laser diode and the fiber to improve the light coupling. Afterward, the light propagates through different liquid phantoms with different scattering coefficients (no absorber) or different absorption coefficients (no scatterer). The light was collected by another fiber with a diameter of 1 mm. This fiber was connected to a power meter (Thorlabs S121C) which was used to detect how much light could be collected from the fiber. Last but not the least, two fibers were attached on the surface of liquid phantoms with a fixed distance of 6 mm. The reason for attaching on the surface is when implementing the experiments in the future, the fiber will be placed on the surface of tissue rather than deep inside. The fiber detecting light can be used to mimic where the ultrasound focus is, however, a fixed distance of 6 mm was used due to the weak laser light power. When doing the transmitted light as a function of scattering

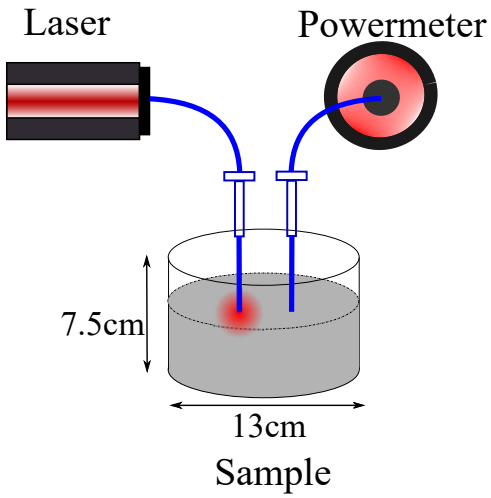

Figure 3.3: Schematic diagram of the transmitted light as a function of scattering and absorption.

coefficient, the increasing scattering coefficient was implemented by keep adding Intralipid 20% from 0.2 ml to 30 ml into the 600 ml water and decreasing the scattering coefficient by diluting pure Intralipid 20%, which means keep adding water from 20 ml to 600 ml into 50 ml pure Intralipid. The transmitted light as a function of absorption was achieved by making phantoms with 5 ml Intralipid and 395 ml water, or with 10 ml Intralipid and 390 ml water, then keep adding ink from

0.1 ml to 6 ml into the phantoms. Afterward, the Enhanced Specular Reflector (ESR) with 98% reflectivity was used to cover the top of the liquid phantoms with incremental scattering coefficient. Two more tests were performed, one was to put the fiber which was connected to power meter deeper and deeper inside the phantoms with a step size of 1 mm and the distance between two fibers was 4.5 mm which is the closest available distance. The other test was to set different distances from 5 mm to 9 mm with a step size of 0.1 mm between the two fibers.

3.3 Spectral hole burning in Pr^{3+}:Y_2SiO_5

The aim for the spectral hole burning experiments is to burn a 1 MHz spectral hole with sharp edges and a good suppression. This part of work can be as preparation work for the UOT.
The crystal used in the experiment was 0.05% doped Pr^{3+}:Y_2SiO_5, and the absorption coefficient for D2, D1 and b polarization at *Site I* were 47 ± 5 cm^{-1}, 3.6 ± 0.5 cm^{-1}, <0.1 cm^{-1} respectively [41] when the temperature was 2 K. However, the empirical value of the absorption coefficient for D2 in the previous experiments was around 20 cm^{-1} [42].
Before the experiments, the principal axes were first determined by looking at the fluorescence since a low absorption coefficient gives a weak fluorescence, but it is hard to distinguish D1 and D2 axis since our eye is more sensitive to weak light and the specific absorption properties of these axes at room temperature were not known. So after the crystal was put in the cryostat, inhomogeneous scans along each axis at 2 K were used to make sure the axis as shown in Figure 3.4.

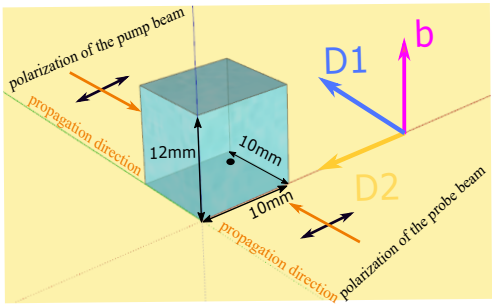

Figure 3.4: A sketch of how the crystal placed in the cryostat with respect to the principle axes, and the light propagation and polarization.

Considering the results of the simulation, burning and probing the crystal along D2 axis was the best choice, which concludes the polarization of the incident beam. After that, a frequency scan was done to find the on-resonance frequency, which around 494.7260 THz.
The experimental setup can be found in Figure 3.5. The laser, coming from a dye laser table [43] with a wavelength of 605.977 nm (494.725 THz) was guided by a polarization-maintaining fiber which preserved the vertical polarization of the laser beam from the complicated dye laser system. This wavelength matched the transition $^3H_4 \rightarrow {}^1D_2$ of the crystal Pr^{3+}:Y_2SiO_5 as mentioned in Figure 2.8. When the laser went through the beam expander, the beam size was diminished from 2.8 mm to 1 mm. The laser was incident onto an Acousto-Optic Modulator (AOM, ISOMET 1205C-2) with the help of mirrors. When the AOM was turned on, the beam split into several orders horizontally. However, only the zeroth and first order passed through while the rest were blocked by an iris. The beam size should keep 1 mm after going through the AOM, but it changed a little bit, and the beam shape became elongated. A beam sampler was located between the beam expander and the AOM. The reflected beam was guided by mirrors and focused onto a reference detector PD1 (Thorlabs, PDB150A) by a lens. This reference signal could be used to eliminate the fluctuations of the laser intensity from the dye laser table.

The zeroth and first order of the AOM could be separated by two mirrors at a far enough distance. The beam size of the first order were 800 μm and 600 μm in the vertical and horizontal direction respectively, which were measured directly after the mirror 6. The first order was transmitted through a half-wave plate, which tuned the laser to horizontal polarization in order to propagate along the D2 axis of the crystal according to the placement of the crystal mentioned at the beginning. A

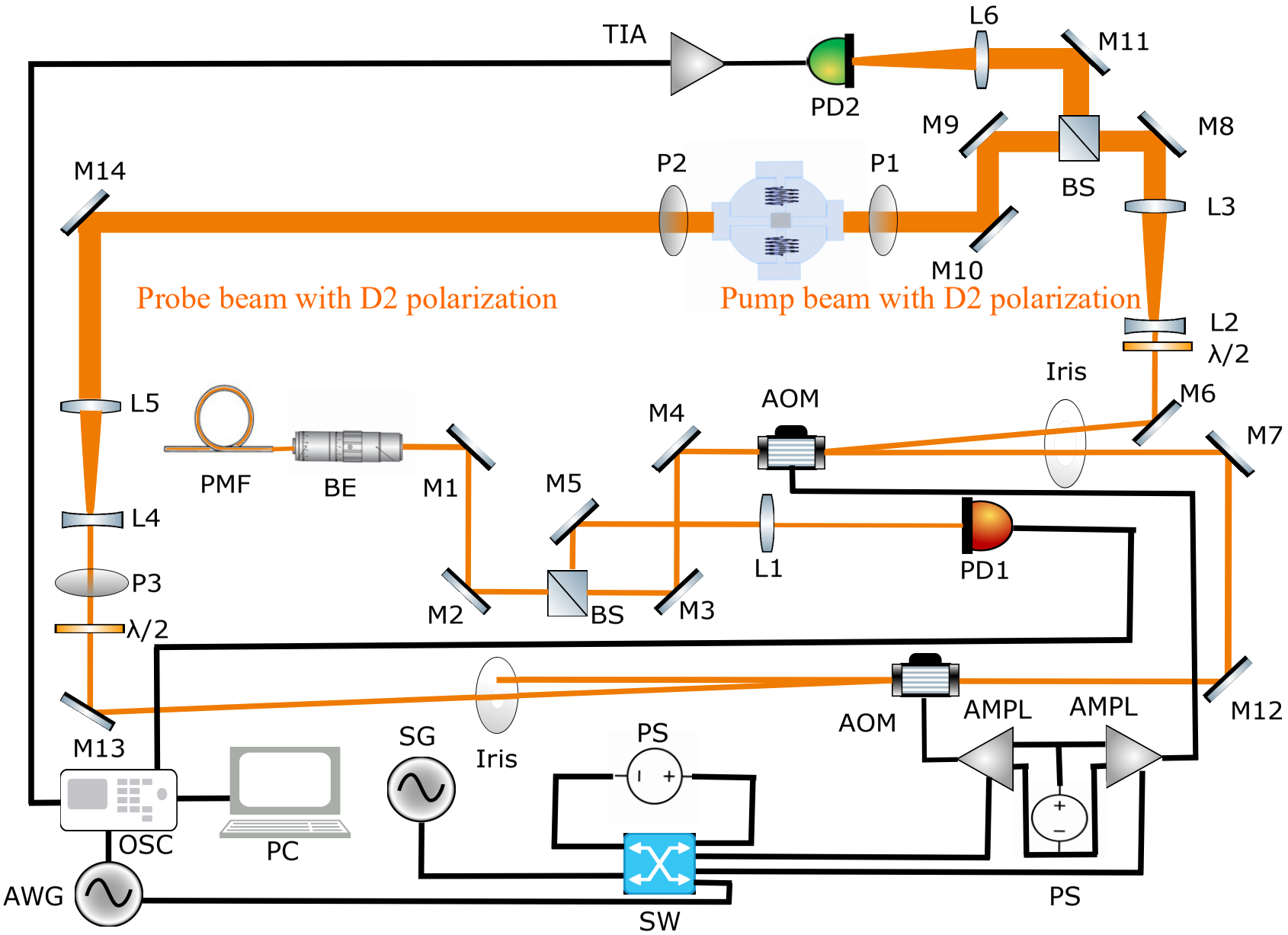

Figure 3.5: Experimental setup of spectral hole burning. AMPL: Amplifier, AOM: Acousto-optic modulator, AWG: Arbitrary waveform generator, BE: Beam expander, BS: Beam splitter, L1-L6: Lens, M1-M14: Mirror, OSC: Oscilloscope, P1-P4: Polarizer, PC: Computer, PD1: Reference detector, PD2: Photodetector, PS: Power supply, PMF: polarization-maintain fiber, SG: Signal generator, SW: Switch, TIA: Transimpedance amplifier, $\lambda/2$: Half-wave plate, the blue one in the middle of pump and probe beam is the cryostat and the crystal sits inside the cryostat.

lens system consisting of a Plano-concave lens (f= -30 mm) and a Plano-convex lens (f= 450 mm) expanded the beam to around 10 mm. A mirror was followed due to the limited space on the optical table to obtain a collimated beam after the lens system. Afterward, a beam splitter with

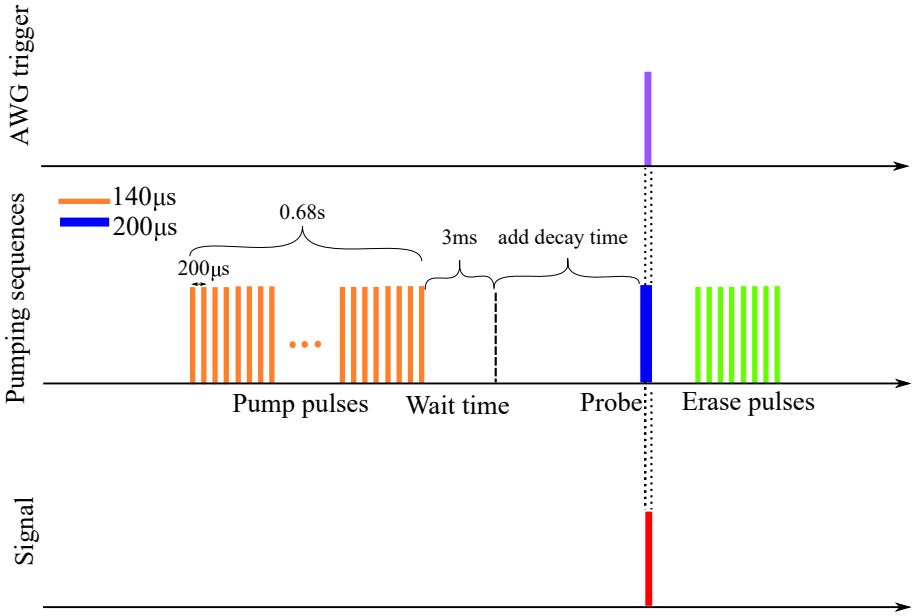

Figure 3.6: A diagram of pumping sequences. Each pump pulse lasted for 140 μs, and the intervals between them were 200 μs. The total time of the pumping sequences was 0.68 s. A 200 μs probe pulse was used for scan readout, and a 3 μs (t_{FWHM}) was used when measuring the suppression due to absorption outside the filter transmission window. A wait time of 3 ms was added between the pump and probe pulse, and more time can be added to see the lifetime of the spectral hole.

90% transmission was used to pump the crystal. The reason why use the first order of the first AOM as a pump beam is the beam path was less. Thence the power was stronger, and the beam shape would be better since the beam only going through one AOM. A polarizer was located right before the cryostat to purify horizontal polarization since the polarization might change because of passing through so many optics. Otherwise, the non-horizontal component would leak into b axis of the crystal, which should be avoided. Still, the polarization might be altered due to the cryostat windows. Thus, another polarizer was placed right after the cryostat. The crystal was confined in a polyether ether ketone (PEEK) holder, and a rod was connected to lower the crystal in the middle of the cryostat such that it could be observed from all four windows. The crystal was cooled down to 2 K inside the cryostat using liquid helium, and a persistent magnetic field could be applied by running a current through the superconducting coil.
The zeroth order of the first AOM was guided by mirrors to the second AOM. Then all the other orders were blocked by the iris except the first order which was used as a probe beam. A half-wave plate and a polarizer were used to turn and purify the horizontal polarization in case of the leakage into b axis of the crystal. Another lens system consisting of a Plano-concave lens (f= -50 mm) and a Plano-convex lens (f= 300 mm) expanded beam to around 10 mm since the beam size just before the lens system were 1800 μm and 1600 μm.

After passing through the cryostat and the beam splitter, 10% of the beam was reflected and focused on the detector (Hamamatsu S5973-02) attached to a trans-impedance amplifier (FEMTO DHPCA-100). The black lines represent cables. The two AOMs were connected to two identical amplifiers which were powered from a single power supply. The AOMs were connected to a switch which was used to select one path at a time. The selection was controlled by the Arbitrary Waveform

Generator (AWG) which sent a trigger to the oscilloscope as well. The oscilloscope was connected to a computer. Therefore, the data from two detectors were saved in the computer via the oscilloscope. When doing the experiments, a pumping sequence was defined as shown in Figure 3.6. The optimized parameters of pump and probe pulse are shown in Table 3.2 to burn a nice 1MHz spectral hole with sharp edges. There are two types of the probe pulse, one for scan readout, where the frequency was scanned from -1 MHz to 1 MHz with a scan rate 100 μs per MHz, and the spectral hole structure could be obtained. The other was for suppression readout, which sent a 3 μs Gaussian pulse in the center of the spectral hole and outside the center of the spectral hole 1.5 MHz away respectively. 1.5 MHz is the central frequency of the ultrasound. The beam diameter of the Gaussian pulse was 5 mm since the laser intensity is not strong enough to generate a detectable signal for larger beam diameters even when using the largest gain of the trans-impedance amplifier. At last, erase pulses were used to fill the hole back to the initial state. Besides, the slow light effect can be inferred after the probe pulse passing through the spectral hole. Furthermore, the lifetime effect of applying a small magnetic field was investigated by adding more wait time between the pump and probe pulses, and the absolute transmission through the hole was also tested. Also, the beam profiler was used to check if the crystal was pumped evenly in the spatial dimension since both the pump and probe beam were quite large.

Table 3.2: Optimizing parameters of pump and probe pulses

Pulse type	Rabi frequency (kHz)	FWHM of the pulse in time (μs)	Frequency scan width (MHz)	Inversion region width (MHz)	Number of pulses	Pulse duration (μs)
Pump	4.6	8	0.92	0.08	2000	140
Probe(Scan readout)	3.6		2		1	200
Probe(Suppression readout)	3.6	3			1	30

Chapter 4

Results and Discussion

4.1 Absorption spectroscopy

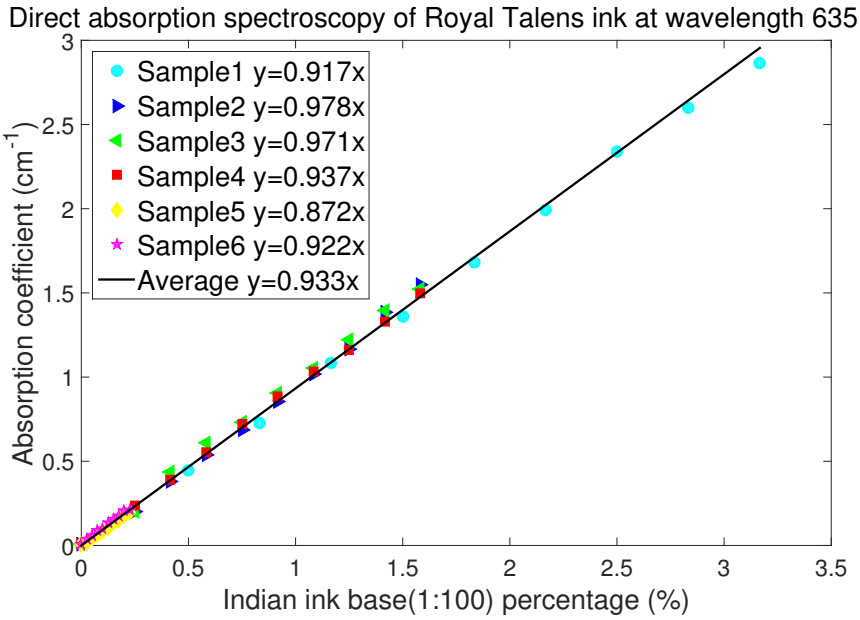

Figure 4.1: Relation between the absorption coefficient and ink base (1:100) concentration.

The direct absorption spectroscopy is a more concise experiment, and it is used to validate the PTOF spectroscopy which is a more complicated method. However, the PTOF spectroscopy can give the exact value of both scattering coefficient and absorption coefficient. The validation of the scattering coefficient for different Intralipid concentration was done by comparing the PTOF measurements with the theoretical scattering coefficient of Intralipid 20% using Equ. 2.4 in [44]. From six groups of measurements, the direct absorption spectroscopy has 11% variation. There is a linear relation between the ink base (1:100) concentration (%) and the absorption coefficient (cm^{-1}) as shown in Figure 4.1. The legend of the figure gives a linear fitting of the experimental data with a coefficient of determination, R^2: 0.9993, 0.9981, 0.9979, 0.9994, 0.9969 and 0.9933 for six groups of measurements. The average coefficient between the ink base (1:100) concentration (%) and the absorption coefficient (cm^{-1}) is 0.933. This method is more suitable for a mediate ink concentration. If the concentration is too low, it is hard to distinguish the difference between the signals with such a small step size. If the concentration is too high, the light would have more

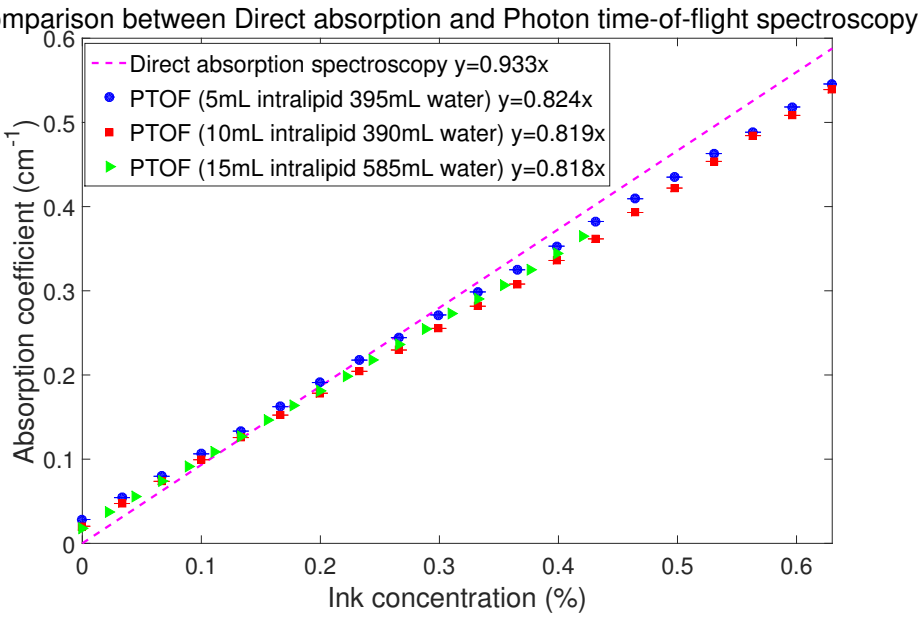

Figure 4.2: Comparison between the direct absorption spectroscopy and the photon time-of-flight spectroscopy.

chance to be scattered. The PTOF spectroscopy is a more precise method, and the error bar is given in Figure 4.2. The effect of the Intralipid and water for the absorption coefficient was also investigated. The reason for the minor difference between the 5 ml and 10 ml Intralipid might be it suffers more reflection from the bottom of the container for the highly scattering phantom. For the phantom of 15 ml Intralipid and 585 ml water compared to the one with the same concentration of Intralipid but less volume, more water gives slightly more absorption coefficient. The separation between two fibers might cause some error for the difference between the PTOF spectroscopy and the direct absorption spectroscopy. The difference can also come from the reflection from the side or the bottom of the container, while it is assumed as an infinite medium in the data evaluation. In addition, the weak light coming out of the source fiber can be influenced by the ambient light more easily as compared to direct absorption spectroscopy.

4.2 Transmitted light as a function of scattering and absorption

Since Monte Carlo simulations match the measurements so well, the MC simulations can be used to mimic the conditions in the UOT experiments, and compare the results with the real experiments.

The output power with error bar varies with the increasing scattering coefficient as shown in Figure 4.3, and it decreases with accumulating absorption coefficient as given in Figure 4.4. These measurements matched the MC simulations. The absolute output power with ESR film and without were tested by keeping adding Intralipid as shown in Figure 4.5. Using ESR film can increase the output power almost twice at a proper scattering coefficient. The film can be used in the UOT experiments to enhance the signal when covering the phantoms.

The error bar was obtained from the deviation of several repeated measurements as shown in Figure 4.3, 4.4, 4.5. It might be due to the position of two fibers because the fibers were reinserted for each measurement, and it is hard to know the exact spot attached to the surface of the liquid phantoms, and more detected output power gives more error since the relative error is almost same for different scattering coefficient. The uncertainty of adding Intralipid and ink might cause an

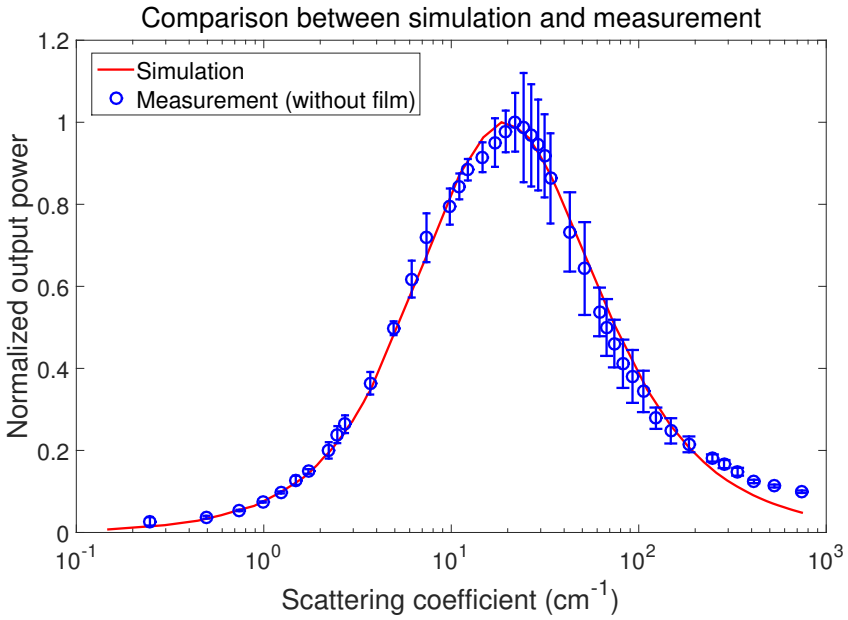

Figure 4.3: Monte Carlo simulations match the measurements for the incremental scattering coefficient.

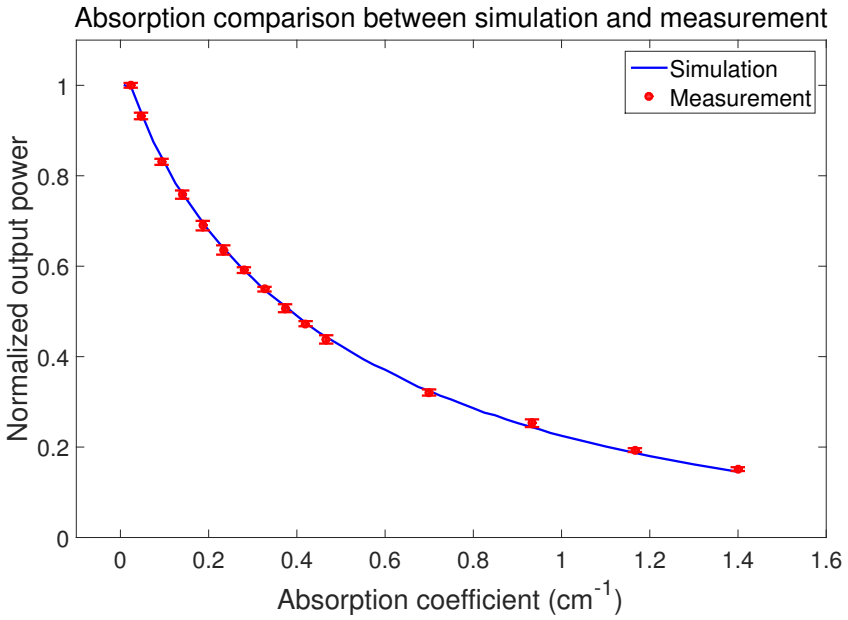

Figure 4.4: Monte Carlo simulations match the measurements for the accumulative absorption coefficient.

error as well. Furthermore, for Monte Carlo simulation, it is assumed to be an infinite phantom. However, in the real case, there are some reflections from the side and bottom of the container especially for the last several groups of measurements where almost pure Intralipid was used, and the volume was small.

Figure 4.6 shows the detecting fiber was placed at different depths while the source fiber was still on the surface, and this is compared to the signal versus fiber separation when two fibers were positioned at the surface. So detecting inside phantoms gives more output power since more photons will escape when attaching on the surface.

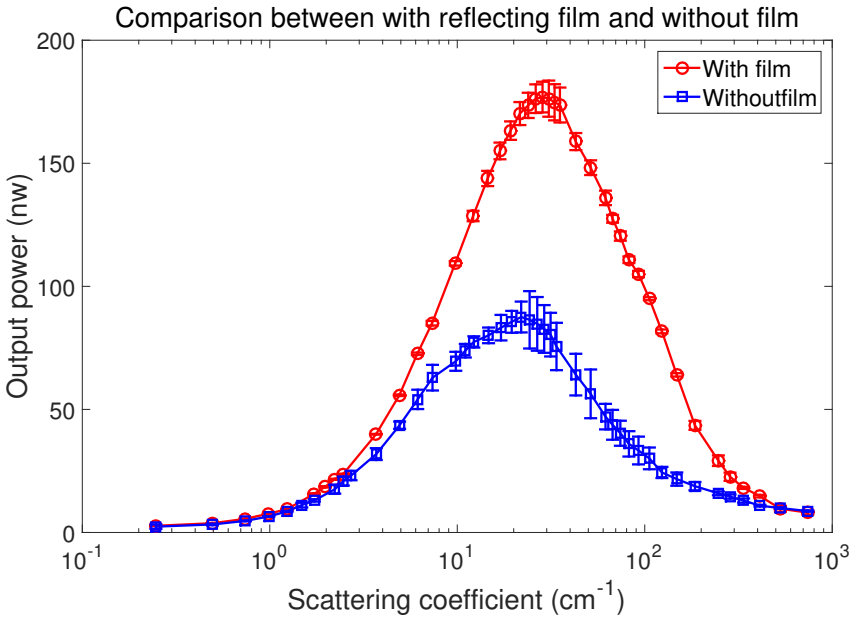

Figure 4.5: The output power comparison between using the ESR film and without when increasing the scattering coefficient.

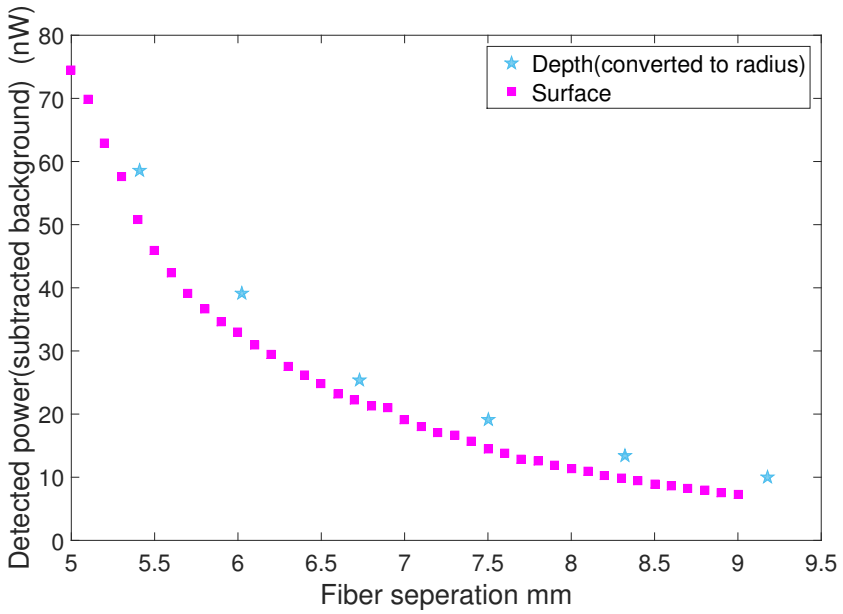

Figure 4.6: The output power for different fiber separations at the surface as compared to that of the detection fiber at different depths.

4.3 Spectral hole burning in Pr^{3+}:Y_2SiO_5

Different wait time is added between pump and probe pulses to acquire the lifetime of the spectral hole without the magnetic field. 0 s, 100 ms, 1 s, 3 s, 6 s, 10 s, and 20 s are the wait time as shown in Figure 4.7. When the transmission drops to 1/e of the transmission without adding wait time, the wait time is between 1 s and 3 s. Therefore, the lifetime of the spectral filter without magnetic field is around 1 s to 3 s.

The lifetime of the spectral hole after applying a small magnetic field of 10 mT is investigated by

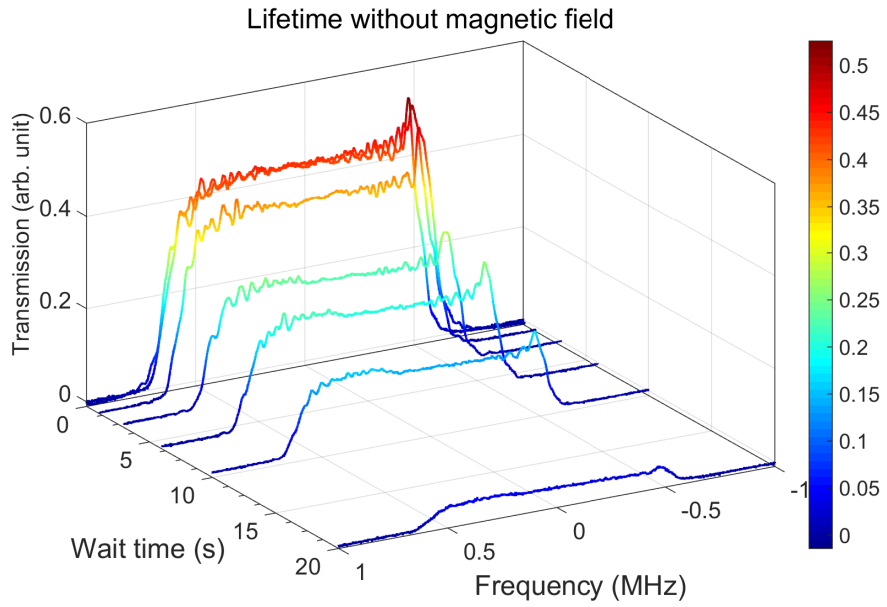

Figure 4.7: The transmission decreases with different wait time without magnetic field. The wait times are 0 s, 100 ms, 1 s, 3 s, 6 s, 10 s and 20 s in turn, so the lifetime of the transmission window without the magnetic field is more than 1s.

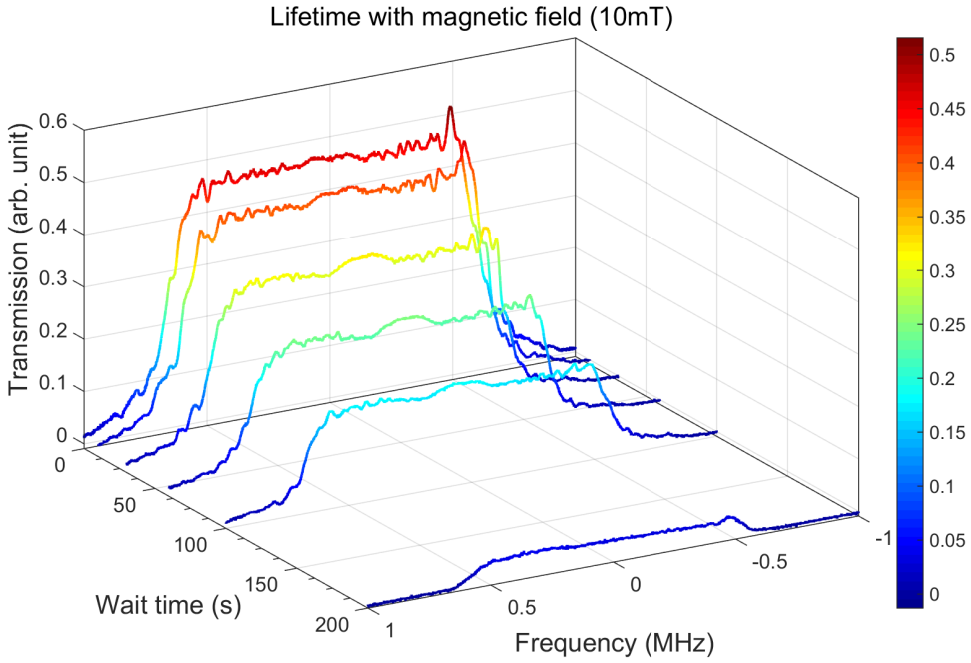

Figure 4.8: The transmission changes with various wait time with magnetic field. The wait times are 0 s, 10 s, 30 s, 60 s, 100 s and 200 s successively, thus the lifetime of the transmission window with the magnetic field is around a half minute to one minute.

adding wait time 0 s, 10 s, 30 s, 60 s, 100 s and 200 s as displayed in Figure 4.8. The transmission decreases significantly between 30 s and 60 s. So the lifetime of the spectral hole can be extended to more than 30 s. However, the spectral hole becomes broader to some extent. The reason for this might be the erase pulses are not efficient enough to fill the hole back, and the spectral hole could last until the pump pulses of the following cycle. For the spectral hole without a magnetic field, it disappears before the pump pulses of the next cycle. It is of importance to extend the lifetime since the data can be collected more efficiently then. More UOT measurements can be implemented after burning the spectral hole once, which then could be accumulated together giving a more accurate signal.

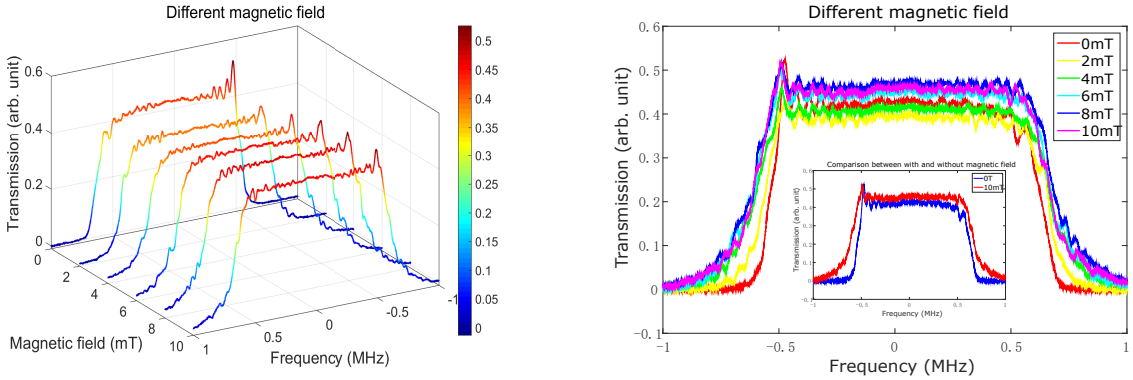

Figure 4.9: The spectral hole fluctuates with different magnetic field with respect to three dimension (right). From a view of two dimension, the transmission increases when adding magnetic field 10 mT and the spectral hole becomes broader (left).

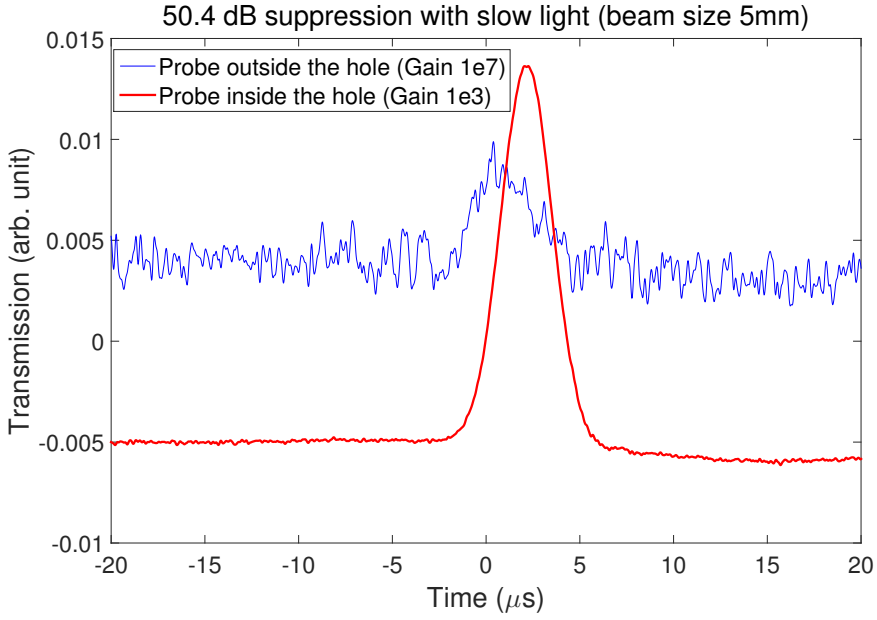

Figure 4.10: Suppression ratio of probing inside the spectral hole and outside the spectral hole with a beam diameter of 5 mm.The different signals can be measured by the detector (PD2) in Figure 3.5 with different gain.

The transmissions with different magnetic fields are also investigated. The applied magnetic field is actually quite small since a larger magnetic field will cause magnetic hyperfine splittings,

which will change the shape of the spectral hole. From Figure 4.3, the transmissions fluctuate with increasing magnetic field from 0 mT to 10 mT with a step size of 2 mT. More detailed information can be seen in Figure 4.3. The transmissions reduce slightly with 2 mT and 4 mT as compared to no magnetic field, and 2 mT magnetic field provides the lowest transmission while 8 mT contributes to the highest transmission. Moreover, the transmissions of 6 mT and 8 mT increase marginally compared with 0 mT. The inset graph shows a growth of the transmission with 10 mT magnetic field as compared to the one without magnetic field. A 10 mT magnetic field will be added in the UOT measurements to extend the lifetime. The transmissions vary a little bit after adding different magnetic fields, whereas the edges of the spectral hole turn out to be not as sharp as without magnetic field. The broadening is caused by the inefficient erase pulses as mentioned above.

The most critical parameter to characterize the spectral hole is the suppression. The red line in Figure 4.10 shows a 3 μs probe light transmitted inside the spectral hole (0 MHz), and the signal was detected with 10^3 gain of the trans-impedance amplifier. Whereas, the blue signal was collected outside the spectral hole (1.5 MHz) with 10^7 amplification. There is a time delay between two signals because the peak of the two signals doesn't coincide with each other due to the slow light effect. The suppression is 44.77 dB without the slow light effect and 50.4 dB considering the slow light effect. The slow light effect can be seen more clearly in Figure 4.11. A 3 μs Gaussian pulse was

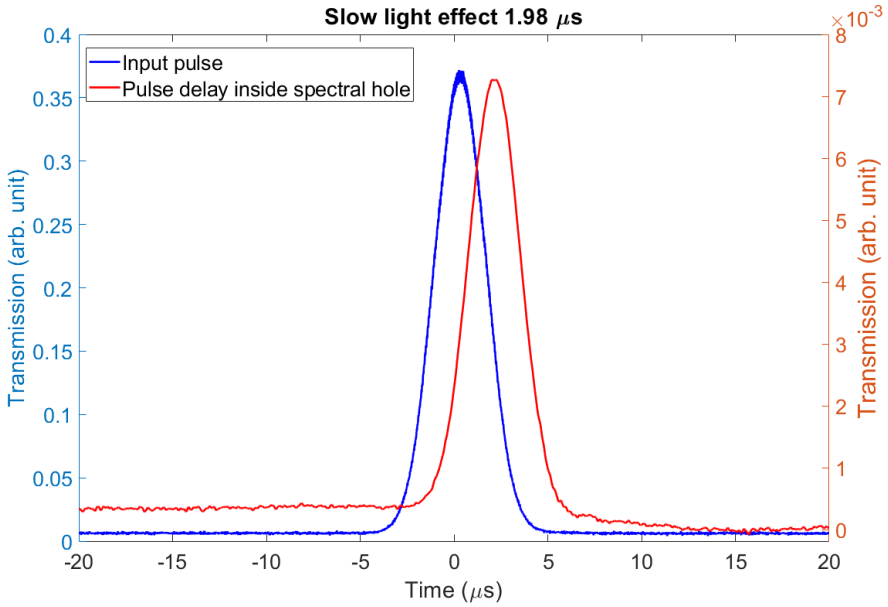

Figure 4.11: The slow light effect for a 1 MHz hole using a 3 μs Gaussian pulse. The blue line can be measured by the reference detector (PD1) in Figure 3.5, while the red line can be obtained from the detector (PD2) of the probe beam.

used to probe, which is represented by the blue line. After propagating through the spectral hole, a time delay of 1.98 μs was obtained, which is specified by the red line. The slow light effect of a 1 MHz hole cannot totally separate an input 3 μs Gaussian pulse and after the spectral hole. This might cause a higher lagging tail on the left side of the red line considering the leakage of the probe beam and the scattered light inside the cryostat. The leakage of the probe beam might come from the unpurified polarization, or some part of the probe light passes through without hitting on the crystal. Therefore, it is better to use a 1 μs Gaussian pulse in the UOT experiments to minimize the leakage of the probe beam and achieve a higher suppression since the input pulse and the probe pulse after the spectral hole can be well separated.

A standard reference was made by setting the maximal pump Rabi frequency (300 kHz), probe

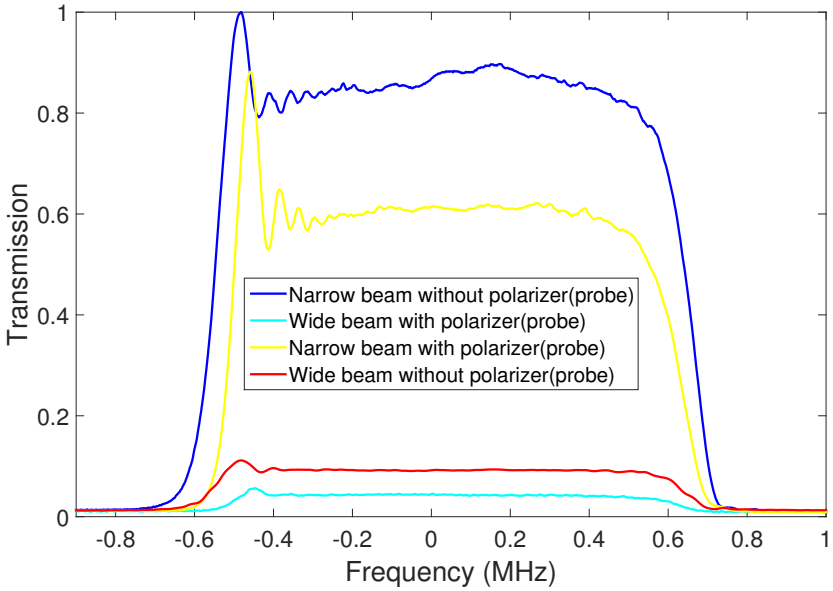

Figure 4.12: An absolute transmission is given by using a standard reference. The blue line is without placing the polarizer in the probe beam right before the cryostat (P2) with a narrow beam, the yellow line is with a P2 and using a narrow beam, the red line using a wide beam but without putting P2, and P2 is located in the cyan line with a wide beam.

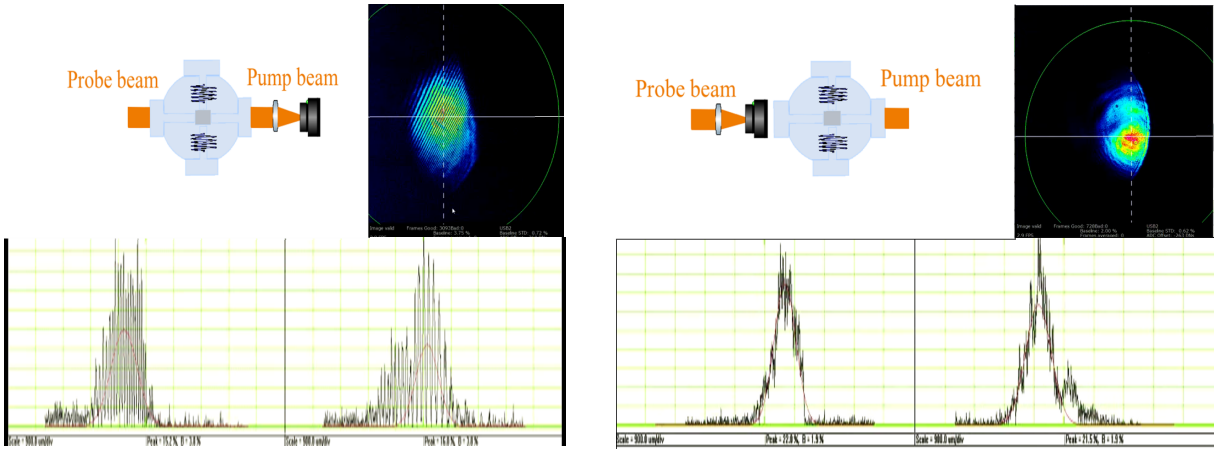

Figure 4.13: A beam profile after probing the crystal is shown in the left part, and the beam profiler is placed directly after the cryostat and block the pump beam. In the right part, a beam profile before probing the crystal is given, and the beam profiler is located before the cryostat. In the left lower part and right lower part correspond to the light distribution of the probe beam along horizontal and vertical directions respectively.

Rabi frequency (2 MHz), the maximum pulse number and using a smaller beam diameter (around 800 μm in vertical and 600 μm in the horizontal direction). However, it is under the assumption that using a narrower beam and the maximal parameters will give a 100% transmission. A polarizer placed in probe beam before the cryostat (P2) or not is also considered. From this method, only around 10.5% of the laser is transmitted through the spectral hole without placing the polarizer, while 7.1% of the laser left after the spectral hole by placing a polarizer. The 32% reduction by setting a polarizer comes from 20% absorption of the polarizer and blocking the polarization component along b axis of the crystal. Therefore, the polarizer blocks around 12% laser light with unpurified

polarization. Nonetheless, this method might not give an accurate value of the transmission since the assumption we made might not be true, and the laser light could be lost due to the cryostat, e.g., the cryostat window. Last but not the least, the beam profile before the cryostat and after the cryostat of the probe beam from a beam profiler and where the beam profiler was put are shown in Figure 4.13. From the beam profile of the probe beam after the crystal, the light distribution is a quite even Gaussian shape, so the spectra hole is burned evenly in spatial. In addition, there are some interferences for the beam profile after probing the crystal, which might come from the front surface of the crystal is not perfectly parallel with the back surface or from the cryostat windows.

Chapter 5

Conclusion and Outlook

This thesis involves three parts of work, making phantoms with specific absorption coefficients and scattering coefficients, test the light propagation inside the phantoms and compare with Monte Carlo simulation, and the spectral hole burning simulations and experiments. For the absorption coefficient work, two methods were used. The direct absorption spectroscopy was based on the Beer-Lambert law and gave a linear relationship between the ink concentration and the absorption coefficient. Thus the average constant between the ink concentration (%) using an ink base (1:100) and the absorption coefficient (cm^{-1}) is 0.9330 as shown in Figure 4.1. The variation of the value is around 11% since neither too low or too high ink concentration works for the direct absorption spectroscopy. For too low concentration, the direct absorption spectroscopy method is not sensitive enough to recognize a small signal change when using an ink base (1:100) with only 0.025% step size as given in Table 3.1. The direct absorption spectroscopy was used to validate another approach Photon time-of-flight spectroscopy since it can provide the scattering coefficient and absorption coefficient of the phantoms at the same time. The PTOF spectroscopy offers 18% difference as compared to the direct absorption spectroscopy shown in Figure 4.2. The difference might come from the distance between the source fiber and the detecting fiber cannot be exactly 20mm. This distance does not affect the absorption coefficient linearly. For the data evaluation part, the White Monte Carlo simulation might not give an accurate result due to the assumption, e.g., infinite medium. Besides, the PTOF spectroscopy is more suitable for the highly scattering and less absorbing phantoms.

The transmitted light inside the phantoms as a function of scattering coefficient and absorption coefficient matched Monte Carlo simulations pretty well. The minor difference between the measurements and Monte Carlo simulations might come from MC simulations don't adequately consider the real conditions, e.g., the reflection from the bottom and the side of the container. The error bar of the measurements caused by the detection fiber was not placed at the same distance and height in different measurements, and it might also generate errors when adding ink and Intralipid into the phantoms. Still Monte Carlo simulations matched the real conditions, so they can be used to simulate the realistic UOT experiments with the help of the full control of the scattering and absorption coefficients. For example, how much light propagates through the ultrasound focus can be calculated by using Monte Carlo simulation, and then compared with the results with the real measurements in the future.

For the third subproject, several spectral hole burning simulations were used before the experiments. The simulations were done to optimize the pulse parameters and number of pulses so that a spectral hole with high suppression ratio and sharp edges can be burned in the experiments. The spectral hole structure can also be investigated where the thickness of the crystal is one thing that is considered. In the experiments, a magnetic field of 10 mT was applied in order to extend the

lifetime of the spectral hole to about a half minute so that the data can be collected more efficiently. Different magnetic fields affected the spectral hole slightly differently. A 1 MHz spectral hole with 50.4 dB suppression by probing inside the center of the spectral hole and outside the spectral hole 1.5 MHz away was obtained considering 1.98 μs slow light effect. Also, the spatial structure of a spectral hole was investigated using a beam profiler. The spectral hole became wide and the edges were not as sharp as after adding a magnetic field. A wider spectral hole might be created because the erase pulses are not efficient enough. Smoother edges might be improved by using the so-called build mountain approach before the burning pulses. The build mountain method is quite useful for a thick crystal to minimize the thickness problem. It requires scanning the laser frequency a broad range, from -45 MHz to -22 MHz and +8 MHz to +32 MHz to pre-burn two spectral holes on the side. Most of the ions from 3/2 state will be transferred to the middle close to the center frequency after building a mountain. If the spectral hole then is burned at the center frequency, the absorption coefficient becomes larger outside the hole, thence gives sharper edges. This build mountain approach is quite interesting to try in the future experiments to burn a sharper spectral hole with a small magnetic field.

References

[1] Sarah E Beavan, Morgan P Hedges, and Matthew J Sellars. Demonstration of photon-echo rephasing of spontaneous emission. *Physical Review Letters*, 109(9):093603, 2012.

[2] Brian Julsgaard, Andreas Walther, Stefan Kröll, and Lars Rippe. Understanding laser stabilization using spectral hole burning. *Optics Express*, 15(18):11444–11465, 2007.

[3] Andreas Walther, Lars Rippe, Lihong V Wang, Stefan Andersson-Engels, and Stefan Kröll. Analysis of the potential for non-invasive imaging of oxygenation at heart depth, using ultrasound optical tomography (uot) or photo-acoustic tomography (pat). *Biomedical Optics Express*, 8(10):4523–4536, 2017.

[4] RN Shakhmuratov, A Rebane, Patrice Mégret, and Joseph Odeurs. Slow light with persistent hole burning. *Physical Review A*, 71(5):053811, 2005.

[5] Qian Li, Yupan Bao, Axel Thuresson, Adam N Nilsson, Lars Rippe, and Stefan Kröll. Slow-light-based optical frequency shifter. *Physical Review A*, 93(4):043832, 2016.

[6] John W Strutt. Xv. on the light from the sky, its polarization and colour. *The London, Edinburgh, and Dublin Philosophical Magazine and Journal of Science*, 41(271):107–120, 1871.

[7] Erik Alerstam. *Optical spectroscopy of turbid media: time-domain measurements and accelerated Monte Carlo modeling*. PhD thesis, lrap-447, Lund Reports in Atomic Physics,Lund University.

[8] Min Xu and Robert R Alfano. Fractal mechanisms of light scattering in biological tissue and cells. *Optics Letters*, 30(22):3051–3053, 2005.

[9] Frank P Bolin, Luther E Preuss, Roy C Taylor, and Robert J Ference. Refractive index of some mammalian tissues using a fiber optic cladding method. *Applied Optics*, 28(12):2297–2303, 1989.

[10] René Michels, Florian Foschum, and Alwin Kienle. Optical properties of fat emulsions. *Optics Express*, 16(8):5907–5925, 2008.

[11] Louis G Henyey and Jesse L Greenstein. Diffuse radiation in the galaxy. *The Astrophysical Journal*, 93:70–83, 1941.

[12] S.A. Prahl. Optical absorption of hemoglobin. `http://omlc.ogi.edu/spectra/hemoglobin/index.html./`, 2006. [Online; accessed 4-March-2018].

[13] RLP Van Veen, Henricus JCM Sterenborg, Antonio Pifferi, Alessandro Torricelli, Ekaterine Chikoidze, and Rinaldo Cubeddu. Determination of visible near-ir absorption coefficients of mammalian fat using time-and spatially resolved diffuse reflectance and transmission spectroscopy. *Journal of Biomedical Optics*, 10(5):054004, 2005.

[14] George M Hale and Marvin R Querry. Optical constants of water in the 200 nm to 200 μm wavelength region. *Applied Optics*, 12(3):555–563, 1973.

[15] John A Parrish. New concepts in therapeutic photomedicine; photochemistry, optical targeting and the therapeutic window. *Journal of Investigative Dermatology*, 77(1):45–50, 1981.

[16] E Antonini and M Brunori. *Hemoglobin and Myoglobin*. Elsevier, 1971.

[17] Edward L Hull and Thomas H Foster. Cytochrome spectroscopy in scattering suspensions containing mitochondria and red blood cells. *Applied Spectroscopy*, 55(2):149–154, 2001.

[18] S.L. Jacques. Optical absorption of melanin. `http://omlc.ogi.edu/spectra/melanin/index.html./`, 2008. [Online; accessed 4-March-2018].

[19] Paola Taroni, Daniela Comelli, Antonio Pifferi, Alessandro Torricelli, and Rinaldo Cubeddu. Absorption of collagen: effects on the estimate of breast composition and related diagnostic implications. *Journal of Biomedical Optics*, 12(1):014021, 2007.

[20] KM Yoo, Feng Liu, and RR Alfano. When does the diffusion approximation fail to describe photon transport in random media? *Physical Review Letters*, 64(22):2647, 1990.

[21] Erik Alerstam, Stefan Andersson-Engels, and Tomas Svensson. White monte carlo for time-resolved photon migration. *Journal of Biomedical Optics*, 13(4):041304, 2008.

[22] Lihong Wang, Steven L Jacques, and Liqiong Zheng. Mcml—monte carlo modeling of light transport in multi-layered tissues. *Computer methods and programs in biomedicine*, 47(2):131–146, 1995.

[23] Erik Alerstam, Tomas Svensson, and Stefan Andersson-Engels. Parallel computing with graphics processing units for high-speed monte carlo simulation of photon migration. *Journal of Biomedical Optics*, 13(6):060504, 2008.

[24] Erik Alerstam, William Chun Yip Lo, Tianyi David Han, Jonathan Rose, Stefan Andersson-Engels, and Lothar Lilge. Next-generation acceleration and code optimization for light transport in turbid media using gpus. *Biomedical Optics Express*, 1(2):658–675, 2010.

[25] Flurin Könz, Y Sun, CW Thiel, RL Cone, RW Equall, RL Hutcheson, and RM Macfarlane. Temperature and concentration dependence of optical dephasing, spectral-hole lifetime, and anisotropic absorption in Eu^{3+}: Y_2SiO_5. *Physical Review B*, 68(8):085109, 2003.

[26] WM Yen, WC Scott, and AL Schawlow. Phonon-induced relaxation in excited optical states of trivalent praseodymium in LaF_3. *Physical Review*, 136(1A):A271, 1964.

[27] RW Equall, RL Cone, and RM Macfarlane. Homogeneous broadening and hyperfine structure of optical transitions in Pr^{3+}:Y_2SiO_5. *Physical Review B*, 52(6):3963, 1995.

[28] Mattias Nilsson, Lars Rippe, Stefan Kröll, Robert Klieber, and Dieter Suter. Hole-burning techniques for isolation and study of individual hyperfine transitions in inhomogeneously broadened solids demonstrated in Pr^{3+}: Y_2SiO_5. *Physical Review B*, 70(21):214116, 2004.

[29] RM Macfarlane and RM Shelby. Coherent transient and holeburning spectroscopy of rare earth ions in solids. In *Modern Problems in Condensed Matter Sciences*, volume 21, pages 51–184. Elsevier, 1987.

[30] Mattias Nilsson. *Coherent interactions in rare-earth-ion-doped crystals for applications in quantum information science*. PhD thesis, lrap-333, Lund Reports on Atomic Physics,Lund University, 2005.

[31] Ying Yan. *Towards single Ce ion detection in a bulk crystal for the development of a single-ion qubit readout scheme*. PhD thesis, lrap-479, Lund Reports on Atomic Physics,Lund University.

[32] Mahmood Sabooni, Qian Li, Lars Rippe, R Krishna Mohan, and Stefan Kröll. Spectral engineering of slow light, cavity line narrowing, and pulse compression. *Physical Review Letters*, 111(18):183602, 2013.

[33] Marlan O Scully and M Suhail Zubairy. Quantum optics, 1999.

[34] `http://qutip.org/docs/3.1.0/guide/guide-bloch.html`. [Online; accessed 30-April-2018].

[35] Axel Thuresson. *Numerical simulations of highly efficient quantum memories*. MSc thesis, lrap-439, Lund Reports in Atomic Physics,Lund University.

[36] `https://uk.vwr.com/store/product/552092/disposable-cuvettes-for-spectrophotometer` [Online; accessed 17-April-2018].

[37] `https://oceanoptics.com/product/hl-2000-family/`. [Online; accessed 17-April-2018].

[38] `https://oceanoptics.com/product/cuv-qpod-temperature-controlled-cuvette-holders/`. [Online; accessed 17-April-2018].

[39] `https://oceanoptics.com/wp-content/uploads/OEM-Data-Sheet-QE65000.pdf`. [Online; accessed 17-April-2018].

[40] `https://oceanoptics.com/product/nirquest512/`. [Online; accessed 17-April-2018].

[41] YC Sun. Rare earth materiais in optical storage and data processing applications. In *Spectroscopic properties of rare earths in optical materials*, pages 379–429. Springer, 2005.

[42] Philip Dalsbecker. *Development of narrow-bandwidth filters for the suppression of scattered light for optical and ultrasound analysis of tissue*. MSc thesis, lrap-502.

[43] Adam Kinos. Light-matter interaction and quantum computing in rare-earth-ion-doped crystals.

[44] Meng Li. *Developing a technique for combining light and ultrasound for deep tissue imaging*. MSc thesis, lrap-546, Lund Report on Atomic Physics, Lund University.

[45] Ronald L Fante. Relationship between radiative-transport theory and maxwell's equations in dielectric media. *JOSA*, 71(4):460–468, 1981.

[46] Mahmood Sabooni, Adam N Nilsson, Gerhard Kristensson, and Lars Rippe. Wave propagation in birefringent materials with off-axis absorption or gain. *Physical Review A*, 93(1):013842, 2016.

[47] Felix R Graf, Alois Renn, Gert Zumofen, and Urs P Wild. Photon-echo attenuation by dynamical processes in rare-earth-ion-doped crystals. *Physical Review B*, 58(9):5462, 1998.

[48] Guokui Liu and Bernard Jacquier. *Spectroscopic properties of rare earths in optical materials*, volume 83. Springer Science & Business Media, 2006.

[49] NM Strickland, PB Sellin, Y Sun, JL Carlsten, and RL Cone. Laser frequency stabilization using regenerative spectral hole burning. *Physical Review B*, 62(3):1473, 2000.

[50] R Orbach. Spin-lattice relaxation in rare-earth salts. In *Proc. R. Soc. Lond. A*, volume 264, pages 458–484. The Royal Society, 1961.

Appendices

A Radiative transport equation

The radiative transport theory (RTT) based on energy conservation in a small volume, can be used to model multiple scattering with the help of the scattering coefficient, scattering phase function and the absorption coefficient, and the radiative transport equation (RTE) states the change of the radiance when the light propagates along $\hat{s}$ direction:

$$\frac{1}{v}\frac{\partial L}{\partial t} = \underbrace{q}_{i)} + \underbrace{\mu_s \int_{4\pi} p(\hat{s}', \hat{s}) L dw'}_{ii)} - \underbrace{\hat{s} \cdot \nabla L}_{iii)} - \underbrace{L(\mu_s + \mu_a)}_{iv)}, \tag{1}$$

where L ($W/m^2 sr$) is the radiance in $\hat{s}$ direction and v is the velocity of transporting energy. The different terms in the right part of the equation corresponds to different events shown in Figure A.1. The first term is the sources inside the volume, the second term comes from the scattering from $\hat{s}'$ direction to $\hat{s}$ direction, the third term results from the boundary exchange and the last term is the radiation loss caused by scattering and absorption. This differential equation totally lacks wave properties [45] and treats the light as in ray optics, however, it is not a problem in diagnostic applications. In spite of the simplifications made, the RTE is still complicated to solve. So two common methods are introduced in the thesis.

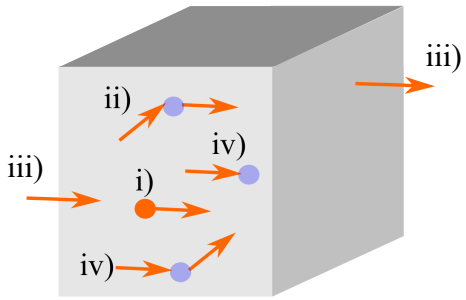

Figure A.1: Radiative transport theory obeys energy conservation in the medium, and the processes involved in:i)Input source ii)Scattering iii)Boundary transition iv)Absorption.

B Host crystal yttrium orthosilicate (Y_2SiO_5)

The host crystal yttrium orthosilicate (Y_2SiO_5) has a monoclinic cell structure which is shown in Figure B.1 with the size of a= 1.041 nm, b= 0.672 nm, c= 1.249 nm, where a, b, c, is the crystal axes, and the b axis is perpendicular to the a-c plane with an intersection angle of 102.65°. Because of the birefringence, the principal axes are slightly shifted from the crystal axes excluding the b axis. The two remaining of axes D1 and D2 lie in the a-c plane with an intersection angle of 79° between the D1 and the a axis. The transition dipole moment is in the plane of D1 and D2 and the intersection angle between transition dipole moment and D1 is 74.6°, which makes the polarization D2 to have the most substantial absorption and on the absorption line the polarization coming out from the crystal will be slightly elliptically polarized when the input polarization is along D2 [46].

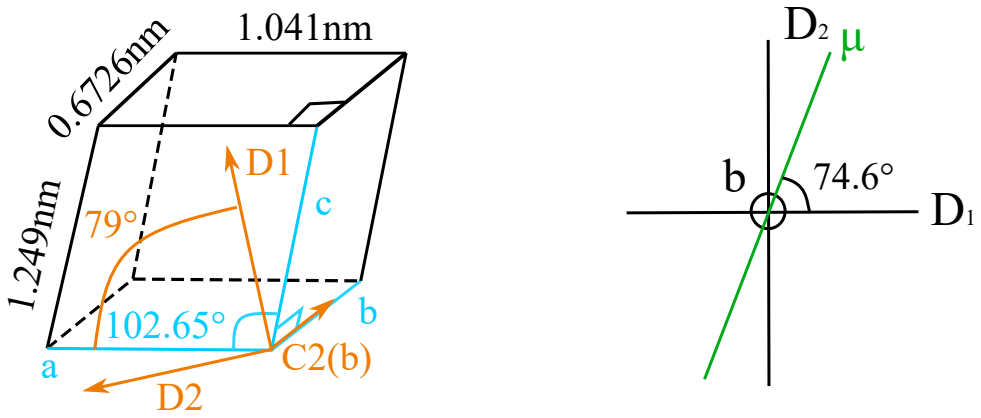

Figure B.1: The crystal lattice structure with crystal axes a, b, c and principle axes D1, D2 and C2 (left). The transition dipole moment lies in the plane of D1 and D2 with an angle of 74.6° compared to D1 (right).

The most abundant isotopes of silicon and oxygen have zero nuclear spins, and the single yttrium isotope has a low nuclear magnetic moment with a nuclear spin of 1/2. This favorable low spin property limits the decoherence effect of the host ions caused by spin flips. Generally, a small fraction of RE^{3+} ions will substitute the Y ions when doped into crystals. There are two separate crystallographically sites which have different absorption coefficient. For Pr^{3+}, the occupation is around 87% at *site I* and 13% at *site II* [29], and *site I* is the focus of this thesis. In addition, the Pr

Parameters	Pr(site I)	Pr(site II)	Ref
λ_{vac}(nm)	605.977	607.934	[27]
ν(THz)	494.726	493.133	[27]
T_1 lifetime(μs)	164	222	[27]
T_2 coherence time(μs)	152(B=7.7mT)	377(B=7.7mT)	[27]
Oscillator strength	$7.7{\cdot}10^{-7}$	$4.5{\cdot}10^{-8}$	[47]
μ_{eg}(C· m)	$2.5{\cdot}10^{-32}$	$6.3{\cdot}10^{-33}$	[47]

Table 1: Spectroscopic properties of Pr^{3+}:Y_2SiO_5, λ_{vac} is vacuum wavelength, ν is frequency, T_1 lifetime and T_2 coherence time is the excited state lifetime and coherence time of the $^3H_4$ and $^1D_2$ transition, Oscillator strength is related to the transition dipole moment and the μ_{eg} represents the transition dipole moment.

ions (*site I*) can interact with laser light strongly, which allows a relatively low laser power to be used

in the experiments. This strong interaction can be described by a large transition dipole moment. The transition dipole moment for Pr^{3+}: Y_2SiO_5 lies in the D1-D2 plane [48]. Combining with the phase retardation effect of the birefringent host crystal, the polarization component of the incoming light has to lie in the D1-D2 plane so that the Pr^{3+} ions can be excited, that is, the absorption of light. Moreover, the light absorption is strongest when the polarization of incoming light is along the D2 axis [46]. Last but not least, some useful spectroscopic data of Pr^{3+}:Y_2SiO_5 is shown in Table 1, more information can be also found in references.

C The coherence time

The long coherence time of 4f-4f transition as mentioned above is quite interesting for quantum memories [30] to put ions in a superposition state and laser stabilization [49]. However, there are processes that could result in decoherence, for instance, the ion-phonon interaction, which changes the energy separation because of the phonon absorption, emission or the phonon scattering[50]. Operating the experiments at a low temperature of 4K can minimize this effect. Other potential complications are, the ion-ion interaction, which shifts the transition frequencies due to variations in electric field and magnetic field, coming from the different electric dipole moments from the ground state and the excited state between two dopant ions and the spin flips between the dopant ions and the host ions respectively. The spin flips can be eliminated by adding a magnetic field. In addition, ion-impurity interaction can broaden the linewidth, and this effect can be diminished by reducing the concentration of dopant ions.